

MICROMAGNETIC SIMULATIONS OF FRUSTRATED
TRIANGULAR ANTIFERROMAGNETS:
APPLICATION TO MAGNETOELECTRIC HoMnO_3

STEPHEN CONDRAN



**Micromagnetic Simulations of Frustrated
Triangular Antiferromagnets: Application to
Magnetoelectric HoMnO_3**

by

© Stephen Condran

A thesis submitted to the
School of Graduate Studies
in partial fulfilment of the
requirements for the degree of
Master of Science

Computational Science Programme
Memorial University of Newfoundland

January 2009

St. John's

Newfoundland

Abstract

Using the Landau-Lifshitz-Gilbert equations, we model magnetic field vs temperature phase transitions in several frustrated stacked triangular antiferromagnets. We find this method to be an improvement from previously used effective field methods.

The algorithm is applied to magnetoelectric HoMnO_3 . A variety of novel interaction terms are proposed to explain the stability of the numerous spin states observed in this and related compounds.

Acknowledgements

I would first like to thank my friends and family, without whom I wouldn't have made it passed my undergraduate degree. In particular, I would like to thank my grandmother Kay, who passed on Christmas in 2008. She has been an inspiration, and was always interested in hearing about what I do, even if she didn't understand.

Also, I would like to thank Martin Plumer, my supervisor, and the rest of the magnetics group at MUN. Their guidance and proofreading will never be forgotten.

Contents

| | |
|---|-----------|
| List of Figures | 5 |
| List of Tables | 6 |
| List of Symbols and Abbreviations | 7 |
| 1 Overview of the magnetic phases in RMnO₃ compounds | 9 |
| 1.1 Our focus | 15 |
| 2 Computational Methods for the Determination of Equilibrium Spin Structures | 18 |
| 2.1 Hamiltonian | 18 |
| 2.2 Computational methods | 23 |
| 2.2.1 Effective Field Method (EFM) | 23 |
| 2.2.2 Landau-Lifshitz-Gilbert method (LLG) | 25 |
| 2.2.3 Comparison of EFM and LLG | 33 |
| 2.2.4 Adaptive time step for LLG | 35 |
| 2.2.5 Addition of temperature to LLG | 40 |
| 3 <i>H-T</i> magnetic phase diagrams: Impact of additional energy terms | 42 |
| 3.1 Identifying phases and transitions | 42 |

| | | |
|----------|--|-----------|
| 3.1.1 | Thermal averages within the LLG formalism | 43 |
| 3.2 | Simple hexagonal systems | 50 |
| 3.3 | AB stacked system with ferromagnetic and anti-ferromagnetic inter- layer coupling | 55 |
| 3.4 | Effect of in-plane anisotropy | 60 |
| 3.5 | Introducing Mn-Ho coupling | 62 |
| 4 | Discussion on the effects of magnetic Ho ions | 65 |
| 4.1 | Simple Landau free energy | 66 |
| 4.2 | More interactions in HoMnO_3 | 67 |
| 5 | Summary and Conclusions | 70 |
| | Appendix: Addition of Temperature to LLG | 72 |

List of Figures

| | | |
|------|---|----|
| 1.1 | The unit cell of RMnO_3 | 10 |
| 1.2 | H-T magnetic phase diagram for HoMnO_3 | 11 |
| 1.3 | In-plane projections of the Mn spins of the HoMnO_3 phase diagram. | 12 |
| 1.4 | Low temperature H-T magnetic phase diagram for HoMnO_3 | 13 |
| 1.5 | The difference between Ho_1 and Ho_2 | 14 |
| 1.6 | H-T magnetic phase diagram as proposed by Yen et al. [3] for TmMnO_3 | 16 |
| | | |
| 2.1 | Effect of the sign of exchange J on square and triangular lattices | 20 |
| 2.2 | Simply to illustrate what θ is. | 21 |
| 2.3 | Two examples of the 120° structure. | 22 |
| 2.4 | EFM for an antiferromagnetic square lattice with $D = -1$ (easy plane). | 26 |
| 2.5 | EFM for an antiferromagnetic square lattice with $D = 1$ (easy axis). | 27 |
| 2.6 | Path of a single spin under LLG dynamics; $\alpha = 0$ | 30 |
| 2.7 | Path of a single spin under LLG dynamics; $\alpha = 0.1$ | 31 |
| 2.8 | Path of a single spin under LLG dynamics; $\alpha = 1$ | 32 |
| 2.9 | LLG for an antiferromagnetic square lattice with $D = -1$ (easy plane). | 33 |
| 2.10 | LLG for an antiferromagnetic square lattice for $D = 1$ (easy axis). | 34 |
| 2.11 | Total computational time of EFM | 36 |
| 2.12 | Total computational time for LLG method | 37 |

| | | |
|------|---|----|
| 2.13 | Total computational time of LLG method with adaptive time step . . . | 39 |
| 2.14 | Average absolute magnetization as a function of temperature | 41 |
| 3.1 | Energy distribution using LLG | 44 |
| 3.2 | S/N vs t for a temperature below T_c | 46 |
| 3.3 | S/N vs t for a temperature above T_c | 47 |
| 3.4 | S/N taken at zero field and varying temperature. | 49 |
| 3.5 | Examples of spins along and perpendicular to basal plane axes | 49 |
| 3.6 | Simple hexagonal or AA stacked lattice | 51 |
| 3.7 | Theoretical phase diagram or simple hexagonal antiferromagnet | 52 |
| 3.8 | Method of finding the transition temperatures. | 53 |
| 3.9 | Phase diagram for simple hexagonal system | 54 |
| 3.10 | Example of an AB stacked hexagonal lattice | 55 |
| 3.11 | AB stacked system with $J_c > 0$ | 56 |
| 3.12 | AB stacked system with $J_c < 0$ | 57 |
| 3.13 | Phase diagram of an AB stacked system with $J_c > 0$ | 58 |
| 3.14 | Phase diagram of an AB stacked system with $J_c < 0$ | 59 |
| 3.15 | Effect of E on an in-plane magnetic spin | 61 |
| 3.16 | AB stacked system with $J_c > 0$ and $E > 0$ | 62 |
| 3.17 | AB stacked system with $J_c < 0$ and $E < 0$ | 63 |
| 4.1 | Landau Phase diagram in zero field | 67 |
| 4.2 | Simple example of exchange on an imperfect triangular lattice. | 67 |
| 4.3 | Possible interactions for HoMnO_3 | 69 |

List of Tables

| | | |
|-----|---|----|
| 3.1 | Empirical values for order parameters W and M | 50 |
| 4.1 | Possible interactions in HoMnO_3 | 68 |

List of Symbols and Abbreviations

| | |
|---------------------------------|---|
| $\vec{S}, \vec{S}_i, \vec{S}_j$ | Spins |
| \vec{P} | Electric polarization |
| \vec{H}, H, H_z | External magnetic field |
| \vec{M} | Magnetization |
| \vec{E} | External electric field |
| \mathcal{H} | Magnetic Hamiltonian |
| t | Time |
| T | Temperature |
| $HT1, HT2$ | High temperature phase 1 & 2 |
| $LT1, LT2$ | Low temperature phase 1 & 2 |
| J_{ij}, J | Exchange interaction between \vec{S}_i and \vec{S}_j |
| J_a, J_c | Exchange interaction between spins in-plane, out of plane |
| D | Single ion anisotropy |
| \hat{c} | Direction of stacked planes of spins |
| \vec{L} | Angular Momentum |
| $\vec{\tau}$ | Torque |
| \vec{r}, \vec{R} | Distance or direction |
| $\vec{\mu}$ | Magnetic moment of an electron |

| | |
|-------------------------|---|
| μ_B | Bohr Magnetron |
| γ | Gyromagnetic ratio |
| EFM | Effective Field Method |
| LLG | Landau-Lifshitz-Gilbert |
| α | Damping constant |
| Δt | Infinitesimal time step, or change in time |
| H_{eff} | Effective Hamiltonian |
| χ^2 | Effective error squared |
| N, L | System size is $N = L^3$ |
| $\eta, \vec{\eta}$ | Random value, vector |
| $\langle M_z \rangle$ | Thermal average of system magnetization along z or \hat{c} axis |
| T_c | Critical temperature |
| E_i | System energy |
| S | 120° order parameter |
| \vec{Q} | Wave vector |
| m, w, M, W | In-plane structure order parameters |
| E_6, E | In-plane anisotropy |
| K | Ho - Mn Trigonal anisotropy interaction |
| $X(t)$ | Time dependent variable |
| $F[X(t), \Delta t]$ | Markov propagator for $X(t)$ |
| $P(X(t))$ | Probability density |

Chapter 1

Overview of the magnetic phases in RMnO_3 compounds

In recent years there has been a revived interest in magnetoelectric phenomena, in particular in the class of compounds RMnO_3 , where R is a rare earth element like Ho, Er, Yb or Y (see Fig. 1.1). Magnetoelectric materials are rather interesting since an applied magnetic field can induce an electric polarization ($\vec{P} \propto \vec{H}$) and an applied electric field can induce a magnetic moment in the material ($\vec{M} \propto \vec{E}$). This behaviour is known as the magnetoelectric effect and occurs in most of these materials at a rather high temperature, on the order of 900K. These materials also exhibit magnetic ordering at a much lower temperature, around 100K for most [1][2][3][4].

This newfound interest in these materials is brought about mostly by academic curiosity but also due to potential applications in industry such as creating a new class of highly accurate sensors, as well as the possibility that these materials will be useful for electronic data storage.

Of particular interest to us in this family is HoMnO_3 which has a complicated low temperature phase diagram, first explored by Fiebig et al. in 2002 using second

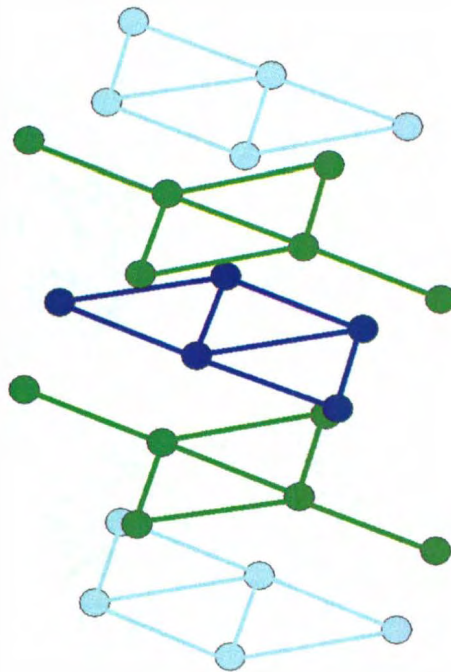


Figure 1.1: Diagram of the unit cell of RMnO_3 . The blue atoms represent the two layers of Mn which make an AB stacked triangular lattice of magnetic spins. The green atoms are the rare earth atoms R which are also on triangular lattices but are AA stacked.[5]

harmonic generation [4]. This diagram depicts a possibility of four low temperature magnetic phases named for their location in the phase diagram. HT1 and HT2 are the so called high temperature phases, occurring between the Néel temperature 75.87 K and roughly 5 K, phases LT1 and LT2 occur at lower temperature.

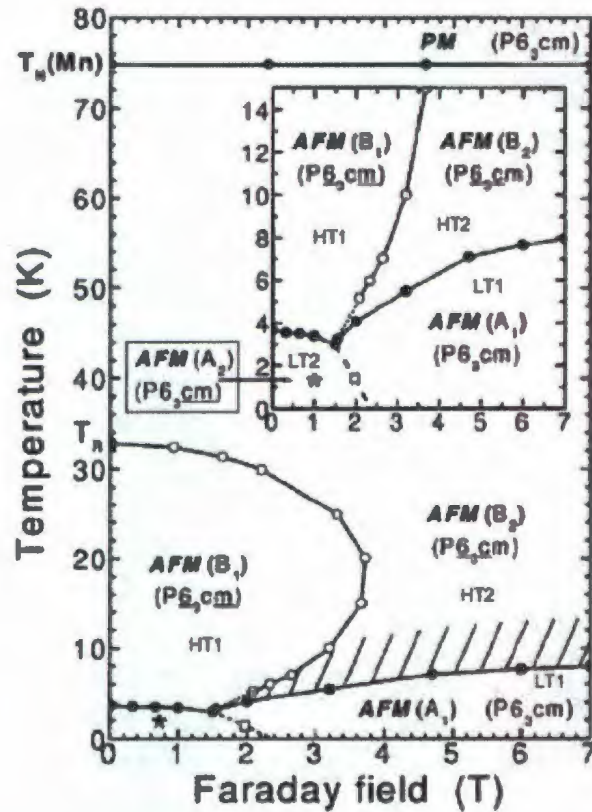


Figure 1.2: Magnetic phase diagram after Fiebig et al. in 2002 [4] using second harmonic generation. There is a switch from a paramagnetic phase to ordered antiferromagnet at $T_N = 75.87$ K to what is known as the high temperature 1 phase (HT1). At lower temperatures starting around 32.5 K, depending on externally applied magnetic fields, HoMnO_3 can take on 3 other antiferromagnetic phases HT2, or low temperature phases LT1, and LT2.

Fig. 1.3 shows the configuration of the Mn spins in each of the four proposed phases by projecting the spins into the plane perpendicular to the \hat{c} axis (remember

that the two layers are stacked in an AB fashion). The lighter colored circles represent the Mn atoms in one layer, while the darker ones represent the second layer in the unit cell. The spins of each phase are either aligned along the basal plane axes as in HT2 and LT2, or the spins are perpendicular to the basal plane axes as in HT1 and LT1. In HT1 and HT2, adjacent layers are ferromagnetically aligned while in LT1 and LT2, the two layers are antiferromagnetically aligned.

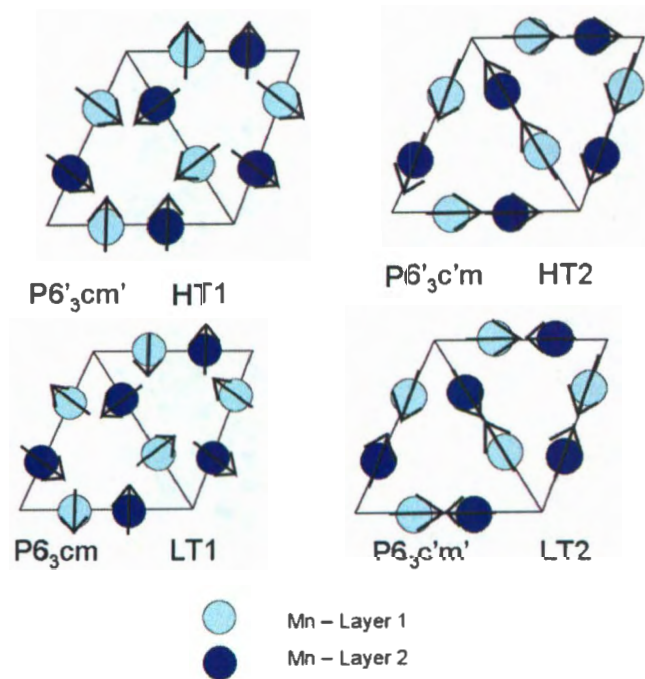


Figure 1.3: In-plane projections of the Mn spins of the HoMnO_3 phase diagram. The dark and light blue circles represent atoms on separate layers. In the HT2 phase all spins are aligned along a basal plane axis and adjacent layers are ferromagnetically aligned. For HT1, all spins are rotated by 90 degrees to become aligned perpendicular to the basal plane axes. LT1 and LT2 are similar to their high temperature counterparts except that the layers are antiferromagnetically aligned.

A few years later Yen et al.[3] found a slightly different phase diagram in which there is an intermediate (INT) phase between HT2 and the zero field line at zero temperature, reducing the LT1 phase to a smaller region at higher field. This phase

diagram is shown in Fig. 1.4.

Early in 2008, Brown and Chatterji [6] used neutron diffraction and proposed a very different view of the phase diagram. They see only one transition at 4.5K and find that the magnetic structure is not affected at all by an external magnetic field. They used a two phase model that defines the magnetic structure at a particular temperature and field as a percentage of the amount of one phase or another are present. In particular, they claim that HT2 and LT2 coexist in the intermediate phase and that their relative proportion depends on H and T.

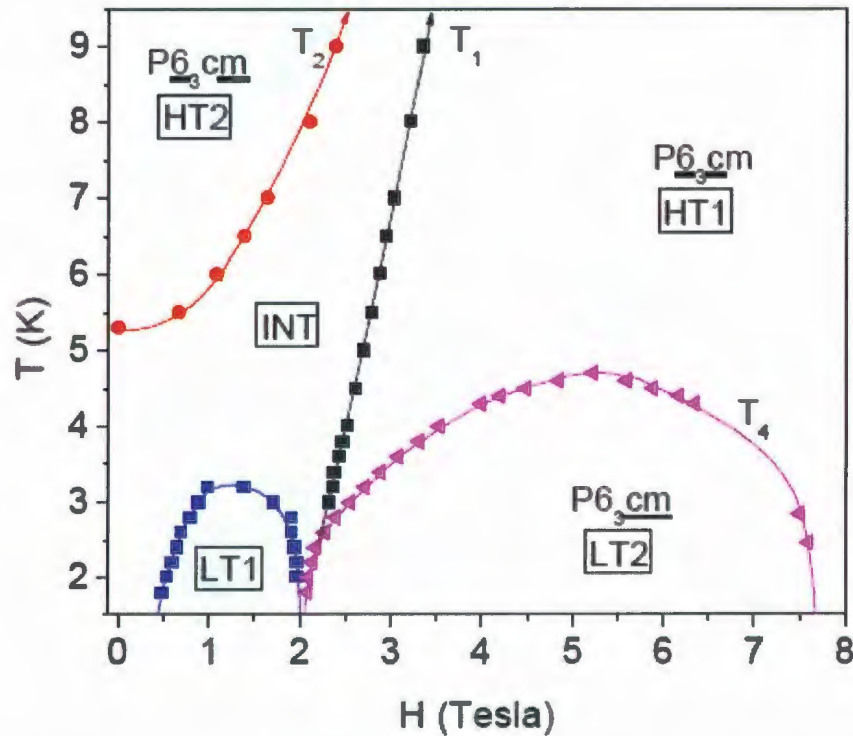


Figure 1.4: Phase diagram of HoMnO₃ reported by Yen et. al.[3], as a part of a study of several members of the RMnO₃ family. The new incommensurate intermediate phase adds to the already rich phase diagram of this material. The other transition temperatures are reported as the same as in previous studies.

However, the Mn are not the only magnetic ions in HoMnO_3 . There is evidence that the Ho ions can also order with spins pointing along the \hat{c} -axis. The ordering of the Ho spins affects, in some way, the ordering of the Mn spins. There are a number of proposals as to exactly how they order, and how the two unlike spins interact. A recent paper by Nandi et al. [7] summarizes the work of several experimental groups regarding the ordering of Ho over a range of fields and temperatures. Their neutron diffraction study finds that the Ho spins are strictly aligned along the \hat{c} -axis and have 2 chemically different subsets, referred to as Ho_1 and Ho_2 , which are respectively white and black in Fig. 1.5. Each of these spins will interact with each other differently due to the arrangement of oxygen atoms around the Ho atoms.

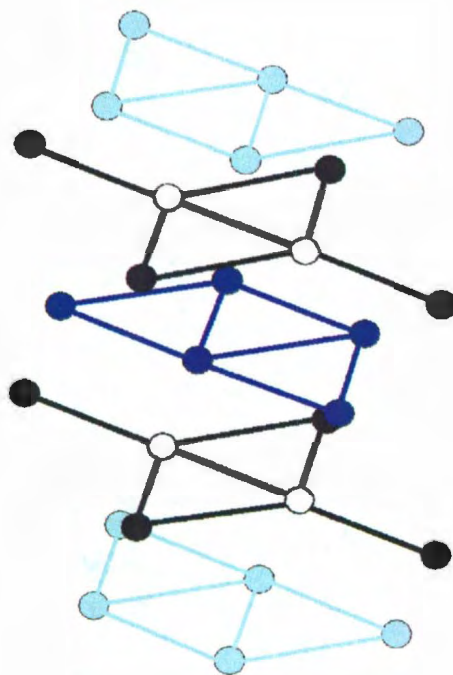


Figure 1.5: The unit cell of HoMnO_3 with Ho_1 as the black atoms and Ho_2 as the white atoms. Even though they are the same atomically, they are in chemically different environments which leads to different magnetic moments and exchange parameters.

They propose that the Ho spins order will change depending on temperature. At high temperature there is a phase where there is no magnetization associated with Ho spins, in terms of the described HoMnO₃ phases this corresponds to the disordered phase and most of the HT1 phase. As the temperature is lowered Ho₁ will begin to order along the \hat{c} axis and Ho₂ will still have no associated ordering, this includes all of the HT2 phase some of HT1. Lowering the temperature further, the Ho spins all order along the \hat{c} -axis, and depending on the strength of an externally applied field, will have Ho₁ and Ho₂ either anti-parallel to one another at low field strength (LT1), or parallel at high field strengths, (LT2) .

While our main interest lies in HoMnO₃, much of what is studied here may be applied to many of the RMnO₃ family by modifying some of the interactions. With a further understanding of this class of materials we might be able to predict and explain many of the diverse phase diagrams. As an example of how the phase diagrams for these materials can differ we have included results for TmMnO₃ in Fig. 1.6. We see that for TmMnO₃ there are only a few ordered magnetic phases, in contrast with HoMnO₃.

Within the family of RMnO₃ it is important to explore all magnetic interactions that might influence the spin structure in order to begin to understand the complexity of their phase diagrams. With this knowledge we might better understand what interactions are important in these materials and how their magnetic structures influence their electrical response.

1.1 Our focus

The goal of a project like this is to completely model the phase diagram of the material of focus and to possibly use the model to understand the phase diagrams

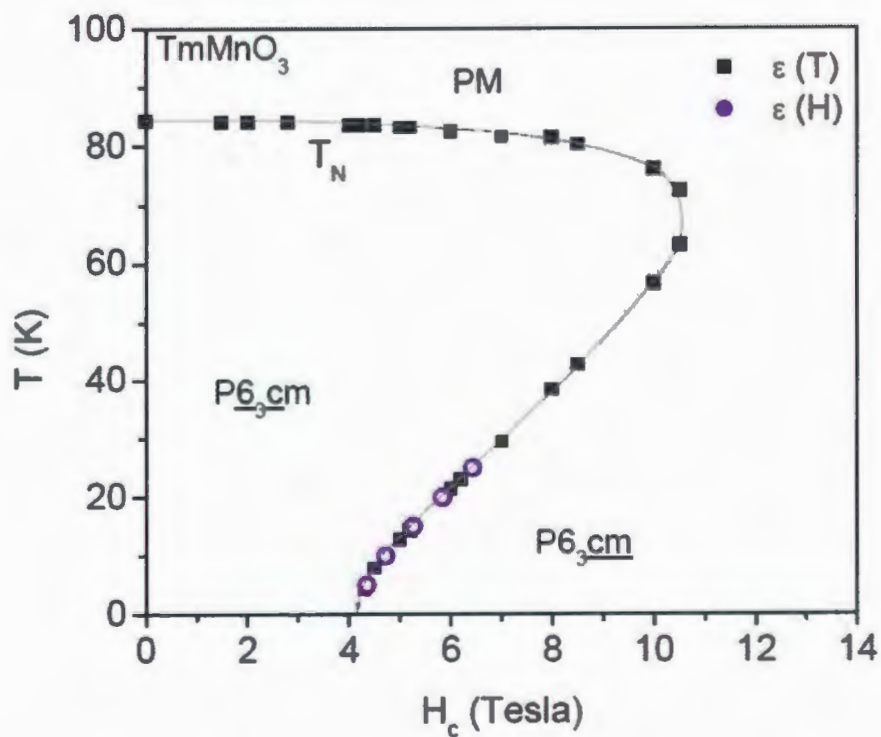


Figure 1.6: TmMnO_3 has fewer phase transitions than HoMnO_3 . They share one magnetic structure, HT2, which is here in the domain closest to zero temperature [3].

of similar materials. If we understand HoMnO_3 and are able to reproduce its phase diagram, we may be able to predict magnetic behavior of many in the RMnO_3 family and explore what is possible for similar materials just by changing the parameters in our model. These are very complex materials and the number and subtlety of can be quite numerous, as we shall see.

The remainder of this thesis is organized as follows. In Chapter 2, we illustrate the origin of a magnetic Hamiltonian for the Mn atoms only, as well as the computational background of our study. We implement and compare two methods with which one can study magnetic systems: the effective field method and the Landau-Lifshitz-Gilbert equations. In Chapter 3, we explore two triangular stacked systems of magnetic spins using the Hamiltonian and methods presented in Chapter 2, and give several simulated phase diagrams. Additional terms to the Hamiltonian are explored and their effects are explained. Chapter 4 is a discussion of the effects of adding the Ho atom interactions to our model, and a simple Landau model free energy is examined. In Chapter 5, a summary of results and some conclusions drawn from this study are presented.

This is the first time LLG equations are used to study the magnetic structures of frustrated antiferromagnets, let alone HoMnO_3 . As such this thesis only lays the ground work that will be needed to reproduce the full experimental H - T phase diagram.

Chapter 2

Computational Methods for the Determination of Equilibrium Spin Structures

The systems described in chapter 1 are complicated, large 3-dimensional hexagonal lattices with many spins per unit cell. To determine the equilibrium spin structures analytically would be virtually impossible. Computer simulations are a faster, easier and hopefully more accurate approach to investigate complicated systems. This chapter describes the methods used to determine spin structures and the phase diagrams of these interesting materials.

2.1 Hamiltonian

A Hamiltonian describes how a system's energy changes with a change of the system's spin configuration. In our case we have a system of unit-length atomic spins on a predefined hexagonal lattice. The goal is to determine the orientation of the spin

vector on each lattice site, \vec{S}_i . Our starting Hamiltonian is defined in equation (2.1). There are three main terms: the first describes the exchange interaction between nearest neighbors, the second is the single-ion anisotropy, and the third is the effect of an external magnetic field.

$$\mathcal{H} = - \sum_{\langle i,j \rangle} J_{ij} \vec{S}_i \cdot \vec{S}_j - D \sum_i S_i^z{}^2 - \sum_i \vec{H} \cdot \vec{S}_i \quad (2.1)$$

In the exchange term, J_{ij} finds its origins with the splitting of the degeneracy of the singlet-triplet ground state of the two electron system [8]. We label it as the effective exchange between two neighboring antisymmetric atomic wave functions that are close enough to overlap. The splitting is caused by the electrostatic energy of the two electrons, as well as the Pauli exclusion principle. These effects cause the degeneracy of the ground state to split into a singlet and triplet state. J_{ij} is due to the energy difference between the two split spin states, $E_s - E_t$.

In the model spin Hamiltonians, J_{ij} is an effective interaction between two magnetic ions depending on the distance between them, so the total energy due to this parameter could be calculated over all ion-spin pairs. However, it drops off quickly, (typically as $e^{-\alpha r}$) so usually only nearest-neighbor (NN) interactions are taken into account, as in our Hamiltonian. Next-nearest-neighbor (NNN) and third-neighbor interactions are sometimes included depending on the specific material of interest.

The sign of J_{ij} dictates how the spins tend to line up as they interact. For example, if J_{ij} is positive, with spins on a square lattice, the spins might line up as in Fig. 2.1A; this is a *ferromagnetic* configuration. Even though J_{ij} causes the neighboring spins to line up in the same direction, it is the other terms of the interaction Hamiltonian that determine the direction of \vec{S}_i relative to the lattice. If J_{ij} is negative on the same square lattice you will get an *antiferromagnetic* configuration, as in Fig. 2.1B.

The lattice in our model system is not square in the xy plane but triangular. Assuming the spins are Ising-like (that is, confined to lie along the vertical y -axis), we can see the effects of $J_{ij} > 0$ and $J_{ij} < 0$ in Figs. 2.1C and 2.1D, respectively. The case of interest is the antiferromagnetic configuration on the triangular lattice as two of the spin pairs can energetically satisfy the anti-parallel alignment while the third spin cannot. Whether it is up or down makes no difference to the energy of the system, making the spin *frustrated*.

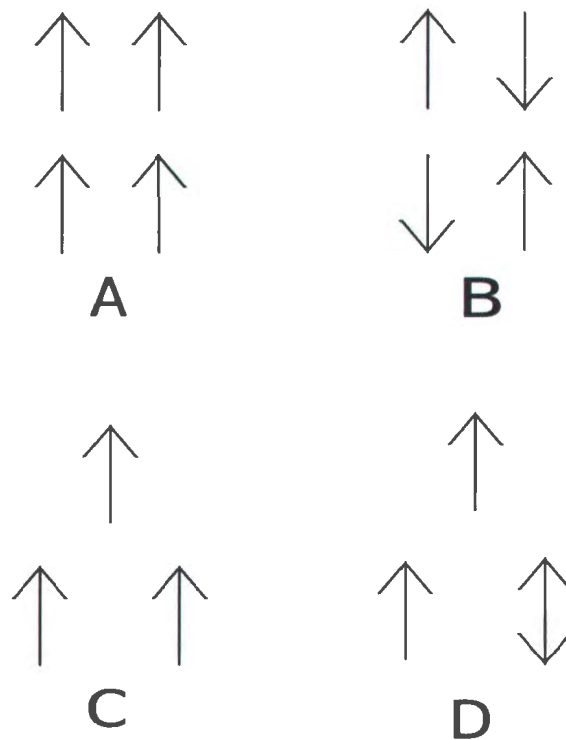


Figure 2.1: Examples of the effect of the exchange interaction sign on equilibrium configurations on a square and triangular lattice for an Ising-like system. For the square lattice examples, (A) has $J > 0$ (ferromagnetic in-plane) so the lowest energy configuration is where all the spins are all spins are parallel, while (B) has $J < 0$ (anti-ferromagnetic in) where instead the lowest energy configuration has all spins are anti-parallel. Triangular lattices are a bit different. Example (C) has $J > 0$ and like the square example all the spins are parallel. However (D) shows a system with $J < 0$ where two spins are anti-parallel, the third spin can be either up or down and still have the lowest energy configuration leading to geometrical frustration.

It is much more interesting when we allow the spins to rotate in the plane. This is called the XY model of magnetic spins. For the exchange interaction we have $\vec{S}_i \cdot \vec{S}_j = S_i S_j \cos(\theta_i - \theta_j)$, where θ_i is the angle \vec{S}_i makes with the \hat{x} axis as shown in Fig. 2.2. Due to the symmetry of the hexagonal lattice, we only need to include three spins in a triangle for NN interactions, which we label S_A , S_B and S_C . As the spins are all nearest neighbors, we take the same J for all spin pairs. We have

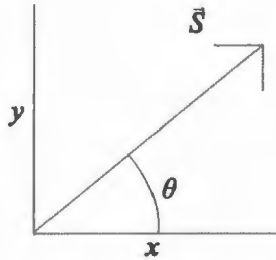


Figure 2.2: Simply to illustrate what θ is.

$$H = -J \sum_{\langle i,j \rangle} \cos(\theta_i - \theta_j) \quad (2.2)$$

$$= -J [\cos(\theta_A - \theta_B) + \cos(\theta_A - \theta_C) + \cos(\theta_B - \theta_C)] \quad (2.3)$$

where $\langle i, j \rangle$ denotes nearest-neighbour pairs only. Now to see what the minimum energy configuration is, we must minimize this interaction Hamiltonian with respect to each of the angles. We get

$$\frac{dH}{d\theta_A} = -J [-\sin(\theta_A - \theta_B) - \sin(\theta_A - \theta_C)] \quad (2.4)$$

$$0 = \sin(\theta_A - \theta_B) + \sin(\theta_A - \theta_C) \quad (2.5)$$

$$2\theta_A = \theta_C + \theta_B \quad (2.6)$$

and from the other two derivatives:

$$2\theta_B = \theta_A + \theta_C \quad (2.7)$$

$$2\theta_C = \theta_A + \theta_B \quad (2.8)$$

There are two possible solutions, $\theta_i = 0$ and a solution where all 3 angles are evenly spaced on the unit circle, that is, $\theta_i - \theta_j = 120^\circ$ as in Fig. 2.3. There are two possible orientations shown, also known as the chirality of the spins. For $\theta_i = 0$, $E_0 = -3J$ and for the 120° spin structure we get $E_{120} = \frac{3}{2}J$. Therefore the 120° spin structure minimizes the exchange energy for $J < 0$. For our model systems on stacked triangular lattices we use two different J_{ij} , one for the interaction between the nearest neighbor spins in-plane, which we called J_a , while for the interaction between nearest neighbor planes along the \hat{c} axis we denote J_c .

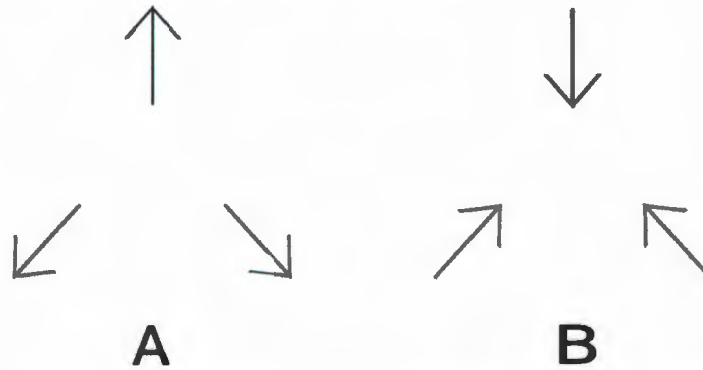


Figure 2.3: Two examples of the 120° structure that are the minimum energy configuration on a hexagonal lattice with $J < 0$ which differ by their chirality.

The single ion anisotropy D comes from spin-orbit coupling. Such a term in the energy is allowed by symmetry for hexagonal crystals. Generally, this creates what is known as the easy axis anisotropy. Depending on the sign of D , this will cause the

spins to align with this axis, or align perpendicular to it. If D is positive the spins will tend to line up with the hexagonal \hat{c} axis, making the system Ising-like (provided that other factors like an external magnetic field do not drive it away from the easy axis). When D is negative, the energy due to D is minimized when the spins lie in the xy plane.

The last term in our Hamiltonian is the so-called Zeeman interaction. H is simply an external magnetic field applied to the system. This term in the Hamiltonian makes the magnetic spins align with this external field. In our calculations, we only consider an applied field aligned with the \hat{c} axis of our hexagonal lattice. This will cause the spins to lift out of the plane when $D < 0$.

2.2 Computational methods

The computational methods we use determine the equilibrium structures of a system of spins depending on the lattice, the exchange, anisotropy, and the external applied field. We will describe two such methods, the Effective Field method (EFM) and Landau-Lifshitz-Gilbert (LLG) equations, but there are many others. For example, there are finite temperature methods that use Monte Carlo algorithms, and other methods that directly minimize the interaction Hamiltonian.

2.2.1 Effective Field Method (EFM)

The EFM is a simple algorithm to minimize the energy of a system of magnetic spins at zero temperature [9]. For each spin, an effective field is calculated by evalu-

ating the negative gradient of the energy (or interaction Hamiltonian as in 2.1):

$$\vec{H}_{\text{eff}} = -\frac{\delta E}{\delta \vec{S}_i} = \sum_j J_j \vec{S}_j + 2D \sum_i S_i^z + \vec{H} \quad (2.9)$$

This effective field represents the local field acting on a spin i , due to the spins around it, the anisotropy, and external applied magnetic field. The local spin energy is minimized if the spin aligns itself with the direction of this effective field. Aligning this spin, \vec{S}_i with its local effective field changes the local field of nearby spins, which in their turn will need to be aligned to this new field to minimize their local energy. Doing this iteratively, the energy of the entire system can be minimized.

The EFM is simple and very quick computationally. First, each spin on the lattice is given a random orientation. The lattice of spins is traversed, examining each spin individually, aligning each with its respective local effective field. This process is iterated a number of times, generally less than one hundred steps, where each pass through the lattice, hopefully brings the system closer to equilibrium.

Unfortunately, with this method it is possible to get stuck in local energy minima, meaning that the equilibrium configuration found might not be the true lowest global energy for those parameters.

To address this issue, the above described method is run tens of thousands of times, each with new randomly generated spin orientations. At the end of each run, the energy of the system is compared to the lowest energy yet achieved; if it is lower, then it is stored as the new minimum energy configuration. After all these runs are complete, hopefully we have the configuration with the true lowest global energy. However, we can never be sure if it is the absolute minimum.

Figures 2.4 and 2.5 illustrate that this method can reproduce the theoretical energy per spin. For each we considered a cubic lattice of antiferromagnetic ($J_a = J_c = -1$)

spins with $D = -1$ (easy plane) and $D = 1$ (easy axis) respectively. We applied a magnetic field \vec{H} parallel to \hat{c} . Theoretically we can find the energy per spin as a function of these parameters. Doing this we find:

$$E = -J\cos(2\theta) - 2D\cos^2(\theta) - 2H_z\cos(\theta) \quad (2.10)$$

where θ is the average angle between the spins and the x axis in the xz plane (similarly shown in figure 2.2). This average is over all spin angles in the lattice. Minimization of the above gives:

$$\theta = \pm \text{Arccos} \left(-\frac{|H_z|}{2(D + 6J)} \right) \quad (2.11)$$

for $|H_z| \leq 2(D + 6J)$. For fields outside this range the energy increases linearly with the field. For $D < 0$ there is a phase transition where the field finally overcomes the effect of D and the spins lift out of the plane. There is no analogous phase transition for $D > 0$: The spins begin anti-parallel, slowly rotating as H_z is increased until they are all aligned along the z axis. As shown in Figs. 2.4 and 2.5, the numerical method is very accurate in this simple case.

2.2.2 Landau-Lifshitz-Gilbert method (LLG)

Another method to determine the equilibrium spin structures makes use of the spin equations of motion and their steady-state solution. This method has been proven to work well for complicated magnetic structures involving long-range dipolar interactions. Consider first how a spin precesses in a field in terms of its angular momentum and how it changes with time. From first year physics we know that classically $\frac{d\vec{L}}{dt} \propto \vec{\tau}$, where \vec{L} is the angular momentum and $\vec{\tau} = \vec{r} \times \vec{F}$ is the torque.

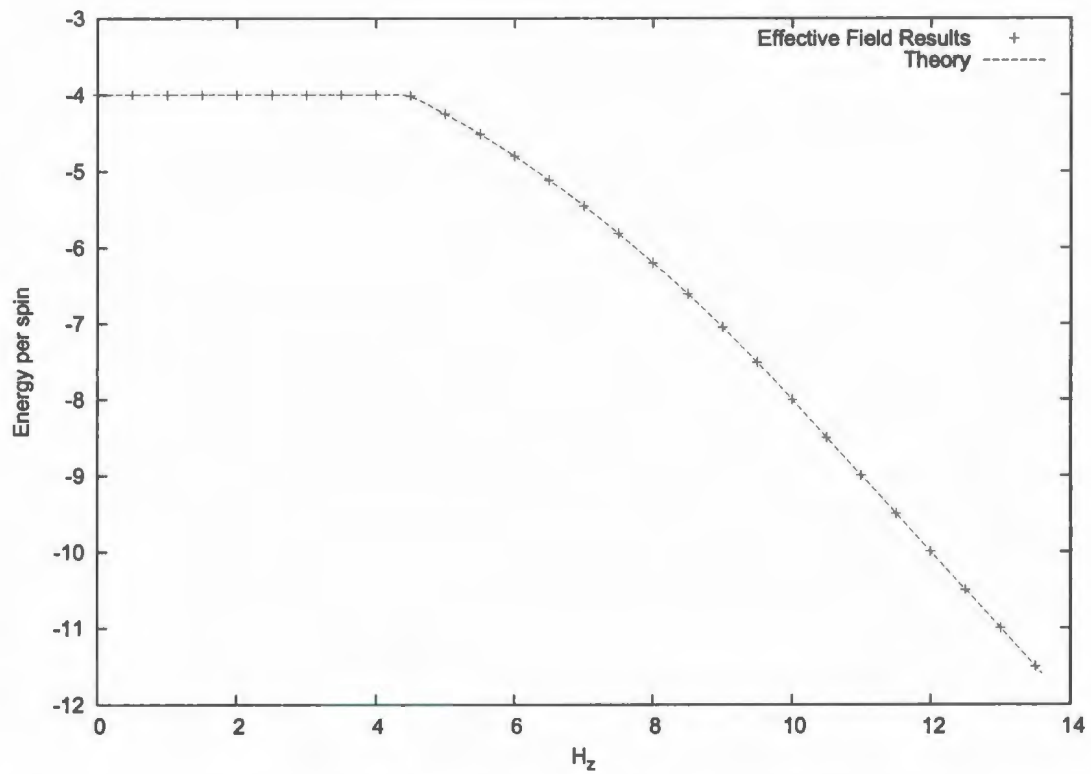


Figure 2.4: Comparison of EFM results to theoretical calculations for energy per spin as a function of applied field H_z using $D = -1$ (easy plane), $N = 12$, $J_a = J_c = -1$ on a cubic lattice. Note that there is a phase transition here at $H_z = 4.0$ where the field is great enough to lift the spins out of the plane.

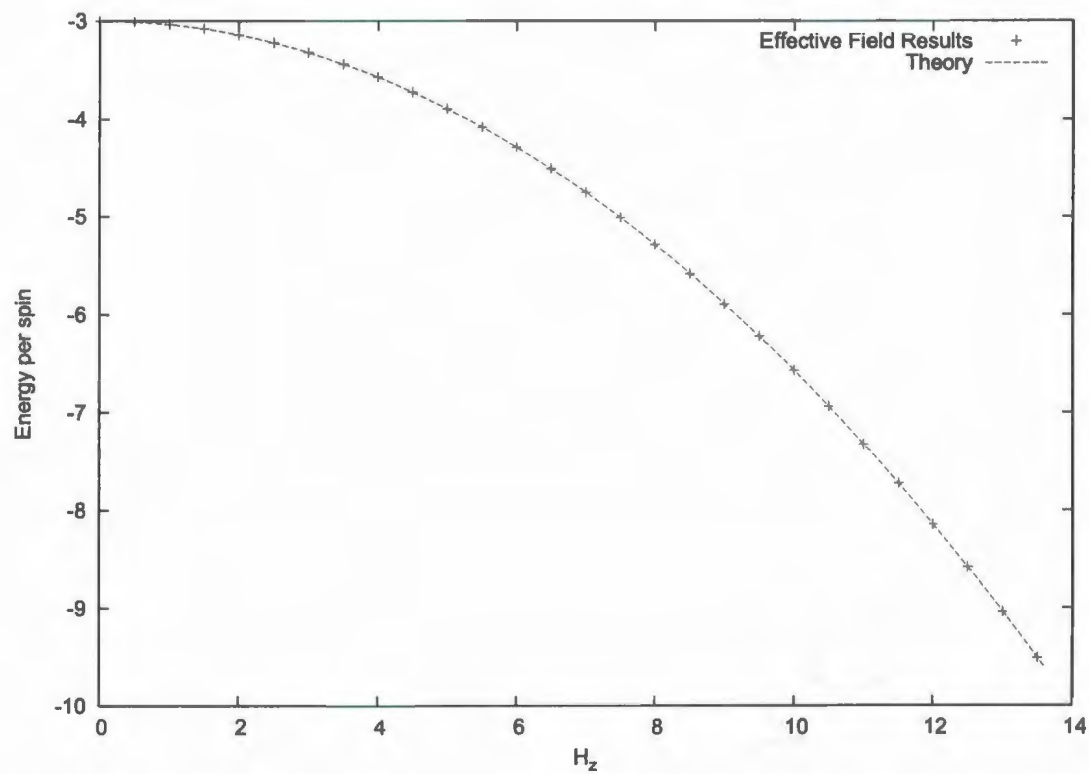


Figure 2.5: Comparison of EFM results to theoretical calculations for energy per spin as a function of applied field H_z using $D = 1$ (easy axis), $N = 12$, $J_a = J_c = -1$ on a cubic lattice.

The torque on an electron due to a magnetic field is $\vec{\tau} = \vec{\mu} \times \vec{H}$ where $\vec{\mu} = \mu_B \vec{S}$ is the magnetic moment of the electron, μ_B is the Bohr magneton, and \vec{H} is an externally applied magnetic field. The angular momentum is related to the magnetic moment by $\vec{L} = \gamma \vec{\mu}$, γ being the gyromagnetic ratio [10]. With this we can construct what are known as the undamped Landau-Lifshitz equation [11]:

$$\frac{d\vec{L}}{dt} = \vec{\mu} \times \vec{H} \quad (2.12)$$

$$\frac{d\vec{\mu}}{dt} = -\gamma \vec{\mu} \times \vec{H} \quad (2.13)$$

$$\frac{d\vec{S}}{dt} = -\gamma \vec{S} \times \vec{H} \quad (2.14)$$

Alternatively we can look at the quantum mechanical spin equation of motion [12]:

$$\frac{d\vec{S}}{dt} = \frac{i\gamma}{\hbar} [\vec{S}, \mathcal{H}] \quad (2.15)$$

where \mathcal{H} is the quantum Heisenberg Hamiltonian. If we now take this into the classical realm (where the commutator becomes a cross product) this becomes:

$$\frac{d\vec{S}}{dt} = -\gamma \vec{S} \times \vec{H} \quad (2.16)$$

which is the same as Eq. 2.14, the undamped Landau-Lifshitz equation.

According to this equation, a spin in a magnetic field would precess endlessly around the the direction of \vec{H} without a mechanism to achieve energy minimization ($\vec{S} \parallel \vec{H}$). In reality, the spins tend to align with the field so we need another term to drive the precession toward the direction of \vec{H} . This is achieved by adding a damping

term to the field in 2.14:

$$\vec{H} \rightarrow \vec{H} - \lambda \frac{d\vec{S}}{dt} \quad (2.17)$$

Substituting this into equation 2.14 and setting $\alpha = \lambda\gamma$ gives:

$$\frac{d\vec{S}}{dt} = -\frac{\gamma}{1+\alpha^2} \vec{S} \times \vec{H} - \frac{\alpha\gamma}{1+\alpha^2} \vec{S} \times (\vec{S} \times \vec{H}) \quad (2.18)$$

Equation 2.18 is called the Landau-Lifshitz-Gilbert equation [14], as Gilbert first suggested a damping term as in Eq. 2.17. For a single spin, \vec{H} represents the external magnetic field, in a lattice of many spins it will become the effective field defined in Eq. 2.9.

Here, α is called the damping coefficient, which dictates how quickly the spin aligns with the effective field. Figures 2.6, 2.7 and 2.8 show the effects of α on the damping of a spin along the x -axis with a magnetic field along z . When $\alpha = 0.0$ the spin precesses around the z -axis indefinitely as there is no damping. For $\alpha = 0.1$, the spin slowly spirals until it aligns with the field. When $\alpha = 1.0$ the spin aligns with the effective field much quicker and achieves energy minimization.

To implement this process in our program we use a simple Euler integrator to evaluate each time step. That is, we approximate $\frac{d\vec{S}(t)}{dt} = \frac{\vec{S}(t+\Delta t) - \vec{S}(t)}{\Delta t}$ and substitute this into the left side of equation 2.18 to get:

$$\vec{S}(t + \Delta t) = \vec{S}(t) - \frac{\Delta t \gamma}{1 + \alpha^2} \left[\vec{S} \times \vec{H}_{\text{eff}} + \alpha \vec{S} \times (\vec{S} \times \vec{H}_{\text{eff}}) \right] \quad (2.19)$$

with Δt being an important parameter to adjust in order to optimize the program. Using the Euler integrator, the error in $\vec{S}(t + \Delta t)$ is proportional to Δt . Also, the larger Δt is the faster the algorithm will run.

Figures 2.9 and 2.10 show the results of the calculated energy per spin of the same

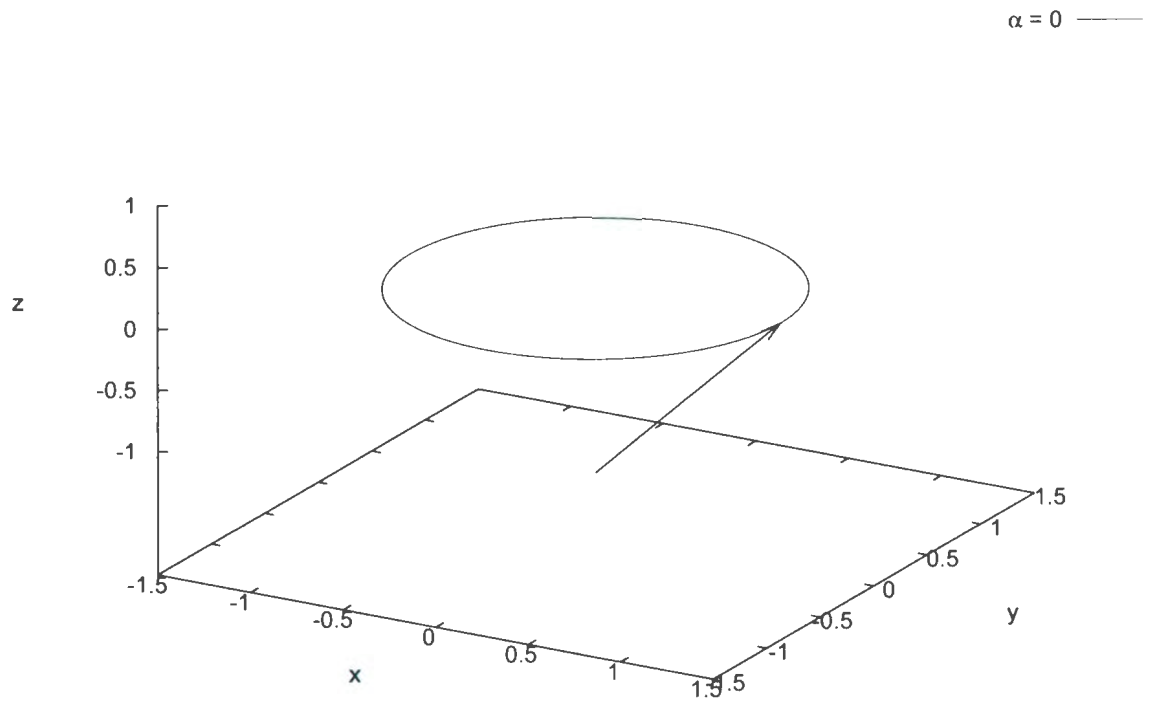


Figure 2.6: Path of a single spin that starts along the x -axis under the LLG equation with $\alpha = 0.0$ and field parallel to the negative z -axis. The spin will rotate in the xy -plane indefinitely.

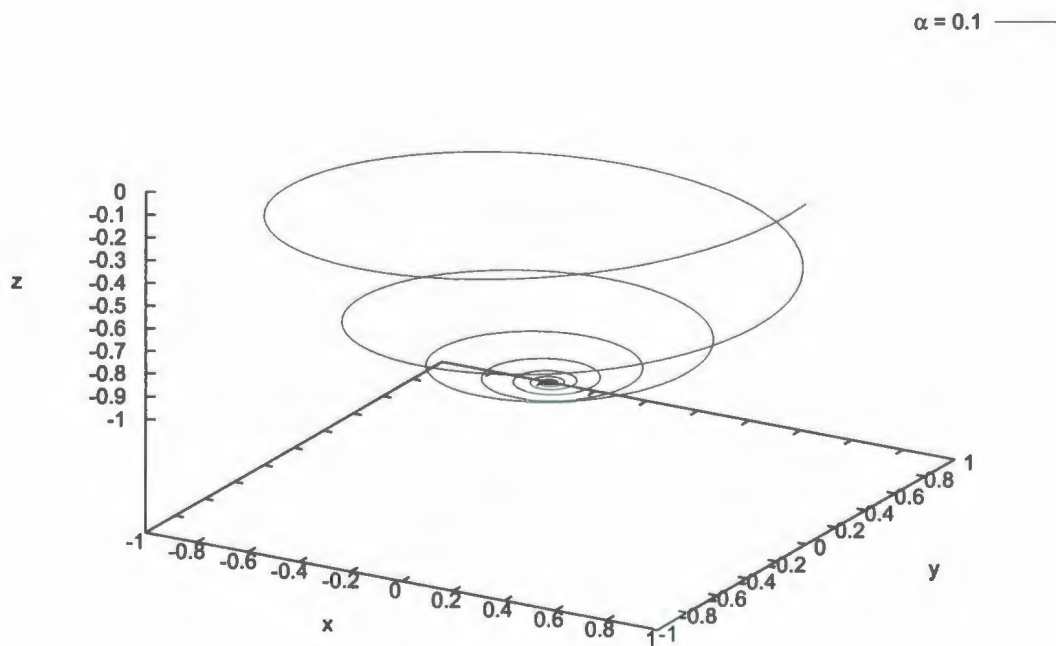


Figure 2.7: Path of a single spin that starts along the x -axis under the LLG equation with $\alpha = 0.1$ and field parallel to the negative z -axis. The spin will slowly spiral down until until the spin aligns with the field.

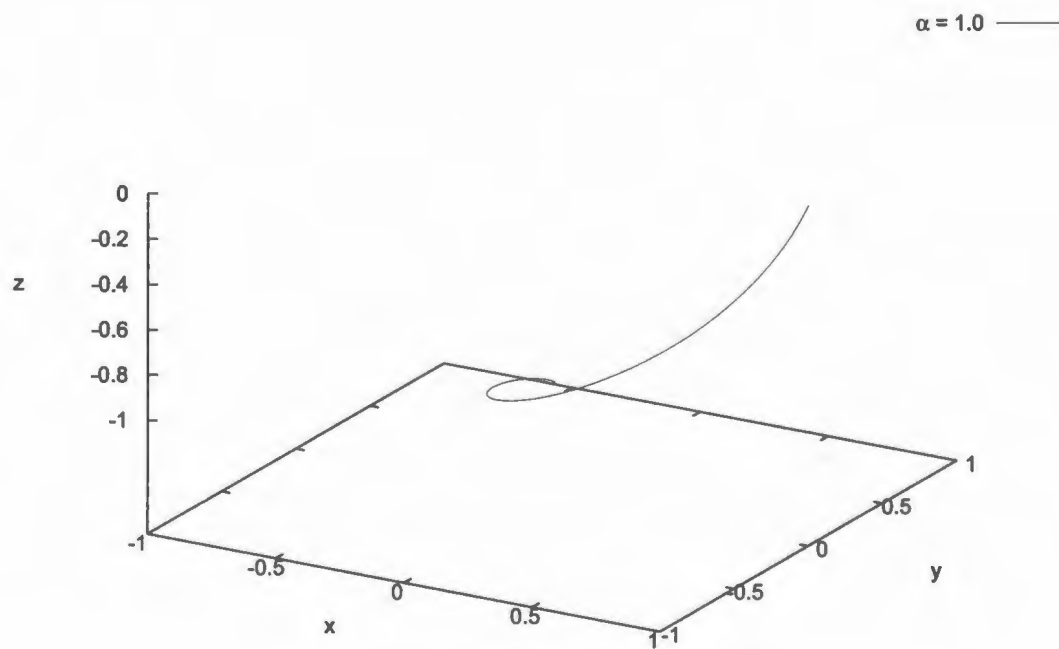


Figure 2.8: Path of a single spin that starts along the x -axis under the LLG equation with $\alpha = 1.0$ and field parallel to the negative z -axis. The spin will quickly align with the field.

system considered for the EFM (Fig. 2.4 and Fig. 2.5). Again the numerical results agrees very well with the theoretical values.

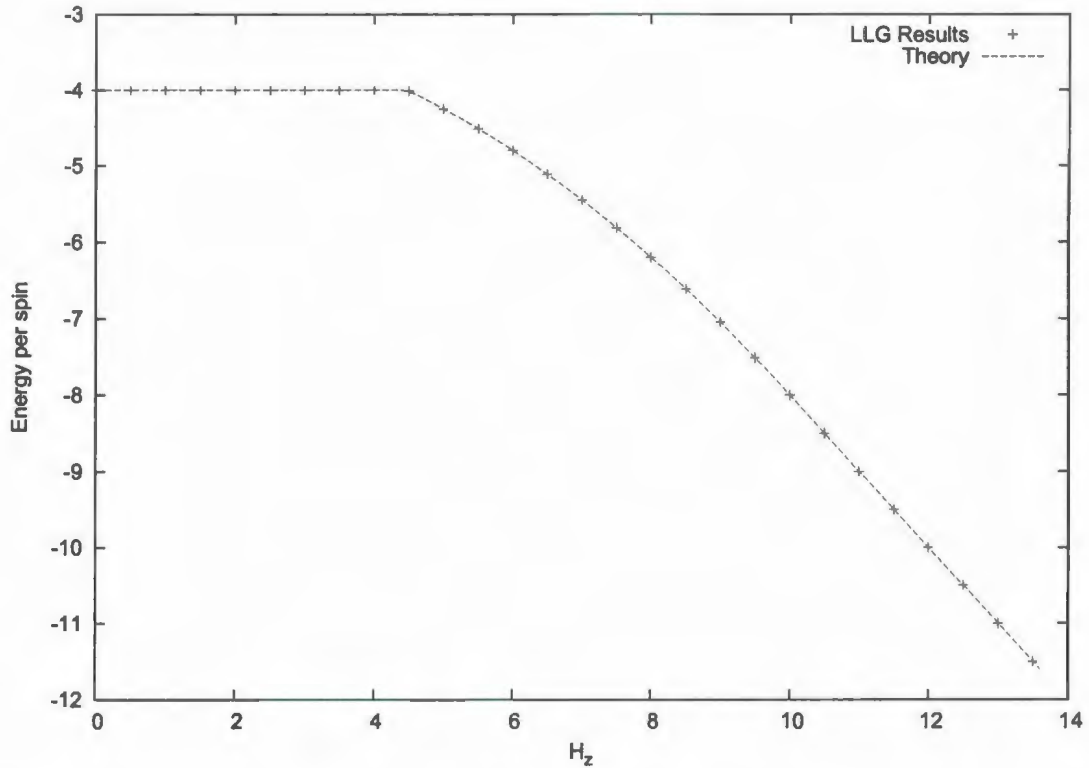


Figure 2.9: Comparison of LLG results to theoretical calculations for energy per spin as a function of applied field H_z using $D = -1$ (easy-plane), $N = 12$, $J_a = J_c = -1$ on a cubic lattice (same as in Fig. 2.4).

2.2.3 Comparison of EFM and LLG

To make a simple comparison between both methods, for accuracy and speed, we used a modified χ^2 test, commonly employed test null hypotheses in statistics. In our calculation, we are testing the difference between the energy per spin between the numerical and theoretical calculation. This includes rounding error, algorithmic error, and error due to the relaxation time. The total of these errors goes like $\sqrt{\chi^2}$,

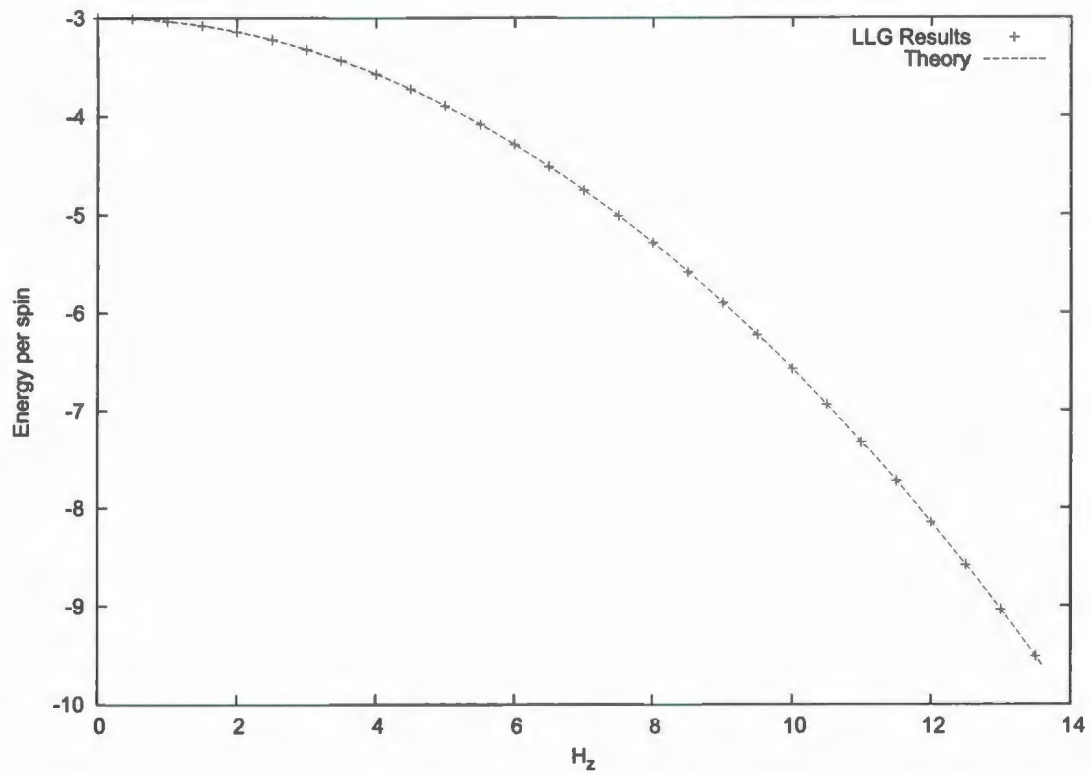


Figure 2.10: Comparison of LLG results to theoretical calculations for energy per spin as a function of applied field H_z using $D = 1$ (easy-axis), $N = 12$, $J_a = J_c = -1$ on a cubic lattice (same as in Fig. 2.5).

and should be a good test for the accuracy of these methods. The form of χ^2 we use is:

$$\chi^2 = \sum_{i=1}^n \frac{(C_i - T_i)^2}{T_i} \quad (2.20)$$

where the sum is over all calculated instances, C_i is the calculated energy per spin, and T_i is theoretical value. Smaller χ^2 means, the closer the numerical result is relative to the theoretical calculation. A reasonable value for χ^2 for either of these algorithms is on the order of 0.01.

The program is run until it reaches a predefined χ^2 threshold and the time is then recorded. Accuracy and computational time are increased by performing more runs for the EFM, or by increasing the total equilibration time in the LLG method.

For our tests we used the same theoretical results as in Figs. 2.4 and 2.9 ($D = -1$, $N = 12$, $J_a = J_c = -1$, and with H_z going from 0 to 14 in steps of 0.5). Each line on Fig. 2.11 shows the total computational time for a different number of passes through the lattice for the EFM while each line on Fig. 2.12 corresponds to a different Δt for the LLG method.

As can be seen from Figs. 2.11 and 2.12, the LLG method is much slower than the EFM in this test. As an example, it takes the LLG method 221 seconds to achieve $\chi^2 = 0.1$ while the EFM requires only 7 seconds. Moreover, the LLG method was unable to converge to the theoretical value for $\chi^2 = 0.03$, which is considered to be insufficient. This problem is addressed by the adaptive time step described in the next section.

2.2.4 Adaptive time step for LLG

Even though the LLG method seems slower than the EFM with convergence of energy, we can improve run times using the so called adaptive time step. Simply put

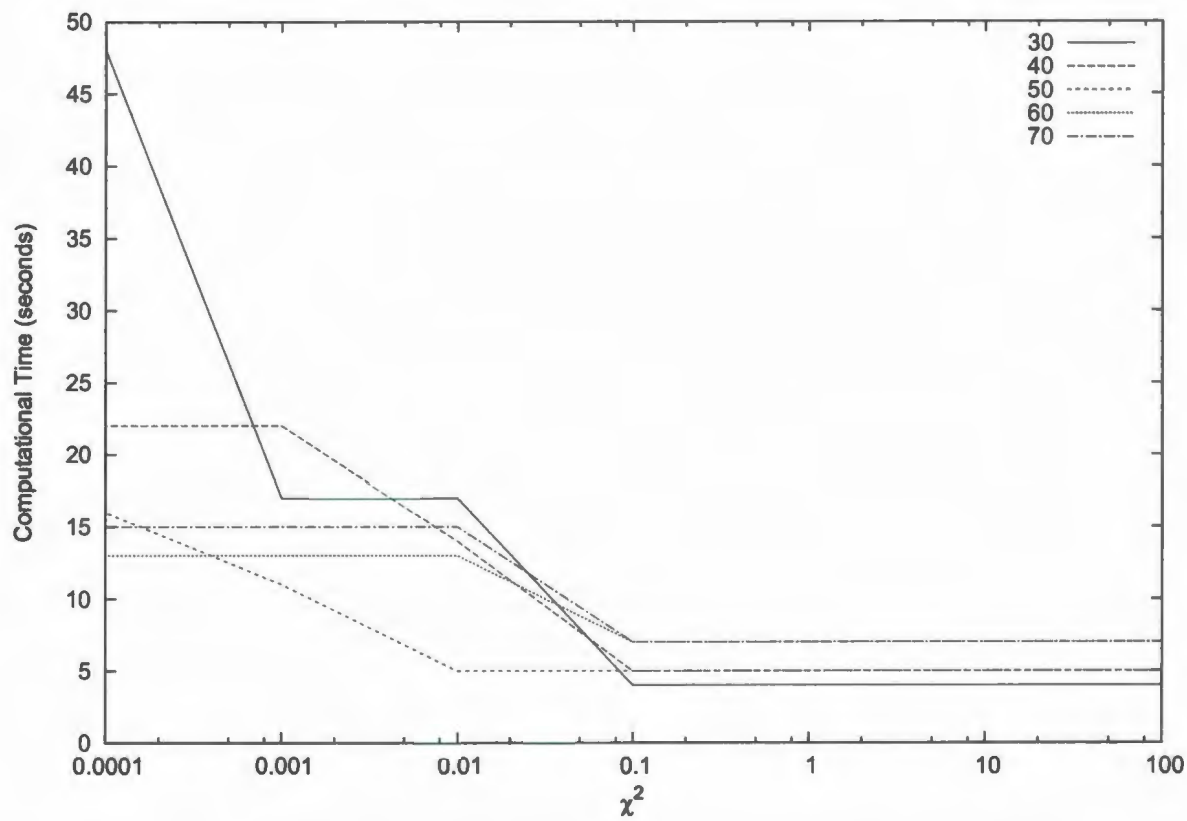


Figure 2.11: Total computational time for convergence of computed energy per spin to the theoretical value for 30-70 passes through the lattice with the EFM. At 60 passes through the lattice the computer energy per spin converges the quickest.

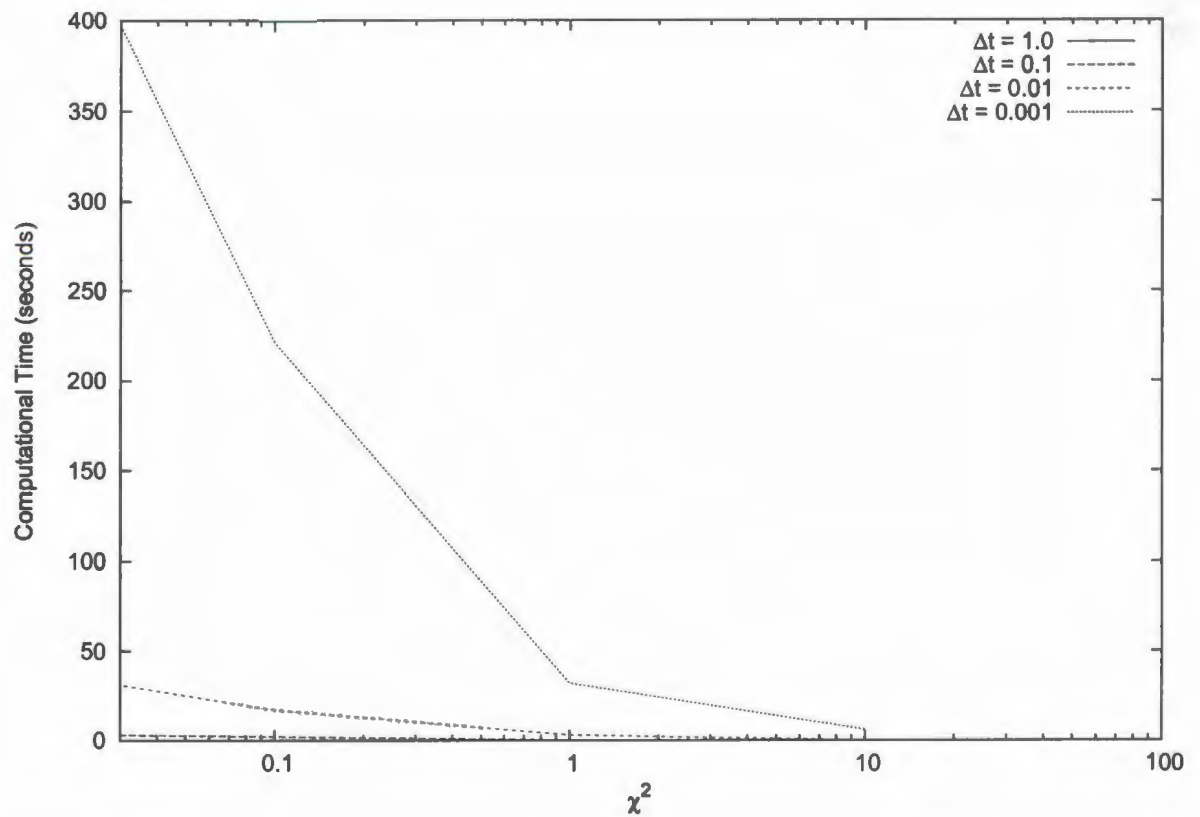


Figure 2.12: Total computational time (note the vertical scale is different than in Fig. 2.11) for the LLG method to converge computed energy per spin to the theoretical value for time step $\Delta t = 0.001, 0.01, 0.1, 1.0$. The case of $\Delta t = 1.0$ is almost parallel to the x -axis.

the adaptive time step is a way to change the size of the time step used in the LLG equation to larger steps when the system is slowly changing and to smaller steps when the system is changing quickly.

This check is a simple energy convergence test. A new spin configuration is generated with a full time step $(t + \Delta t)$ with energy E_1 as well one with a half time step $(t + \frac{\Delta t}{2})$. From the half time step system another system is generated with the half time step $(t + (\frac{\Delta t}{2} + \frac{\Delta t}{2}))$ that has energy E_2 . If $|E_1 - E_2|$ is within some threshold, typically 10^{-2} , the step is accepted and the time step is doubled. If not, the step is rejected, the time step is halved, and the convergence test is done again generating a new spin configuration.

The speed up is substantial using the adaptive time step as can be seen from Fig. 2.13, which is with $\Delta t = 10^{-4}$. The LLG method without the adaptive time step was only able to converge to $\chi^2 = 0.1$, with this particular time step (Δt) there is over a 1500 times speed up at $\chi^2 = 0.1$, as well as achieving greater accuracy.

Now for $\chi^2 = 0.1$, the LLG method with adaptive time step takes only 10 seconds to converge which is on the same order of EFM's 7 seconds. For more complicated spin systems (such as those with long-range dipolar interactions), LLG is expected to be more reliable and faster. Greater accuracy can also be achieved by using a different integrator than Euler such as the mid-point method where

$$\frac{d\vec{S}}{dt} \rightarrow \frac{\vec{S}(t + \Delta t) - \vec{S}(t - \Delta t)}{2\Delta t} + O(\Delta t^2) \quad (2.21)$$

However, the Euler method is considered to be the most straightforward to implement when finite temperature effects are added through a stochastic field term [13] as described below.

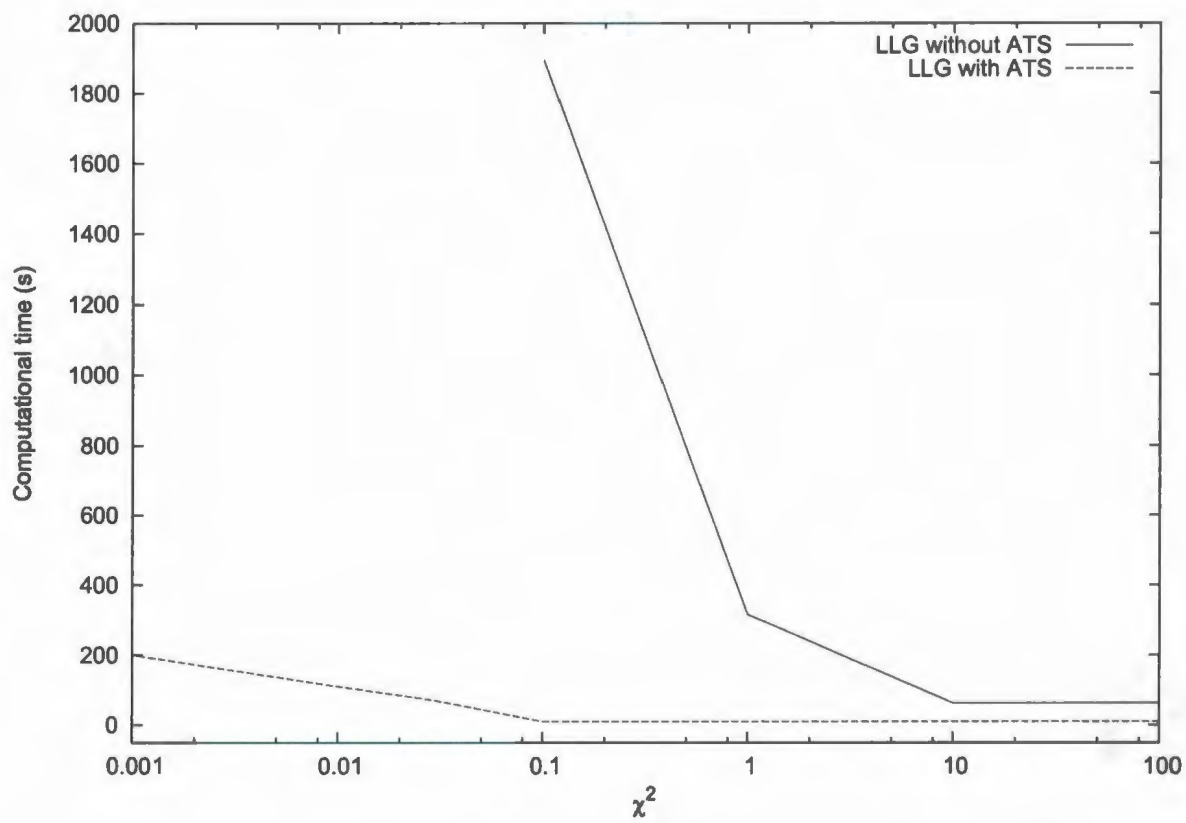


Figure 2.13: Total computational time for convergence of computed energy per spin to the theoretical value for $\Delta t = 10^{-4}$ for LLG with and without adaptive time step(ATS).

2.2.5 Addition of temperature to LLG

To study the phase diagram of the RMnO₃ class of materials, we need to look at how temperature affects the system. Adding temperature to the computational calculations is where the EFM and LLG equations diverge in their usefulness. To simulate temperature a new term is added to the damped LLG equation which represents a small random torque. This new term, explained in Appendix A, and when added to Eq. 2.19 we get:

$$\vec{S}(t + \Delta t) = \vec{S}(t) - \frac{\Delta t \gamma}{1 + \alpha^2} \left[\vec{S} \times \vec{H}_{\text{eff}} + \alpha \vec{S} \times (\vec{S} \times \vec{H}_{\text{eff}}) \right] - \sqrt{\Delta t} \vec{S} \times \vec{\eta} \quad (2.22)$$

where $\vec{\eta}$ is a stochastic field that is due to thermal fluctuations.

The EFM completely fails when a random vector term is added. The EFM fails to represent any sort of dynamic variables, such as temperature, as it is just an energy minimization technique.

To test the LLG method with temperature added, we used a 2 dimensional square lattice of spins of various sizes with $J = 1$, $H_z = 0$, and $D = 1$. Thus, we have an Ising-like system where the average absolute magnetization is measured with respect to the z -axis is measured. There should be a transition to zero magnetization at a critical temperature which we can see in Fig. 2.14. Here $\langle |M_z| \rangle$ represents the thermal average of the magnetization along the z -axis and is defined by

$$\langle |M_z| \rangle = \left| \sum_{i=1}^N S_i^z \right| \quad (2.23)$$

The transition temperature found here, $T_c \simeq 0.8J/k_B$ is in good agreement with previous LLG calculations [13]. A complete discussion of thermal averaging within the LLG formalism is deferred to the next chapter.

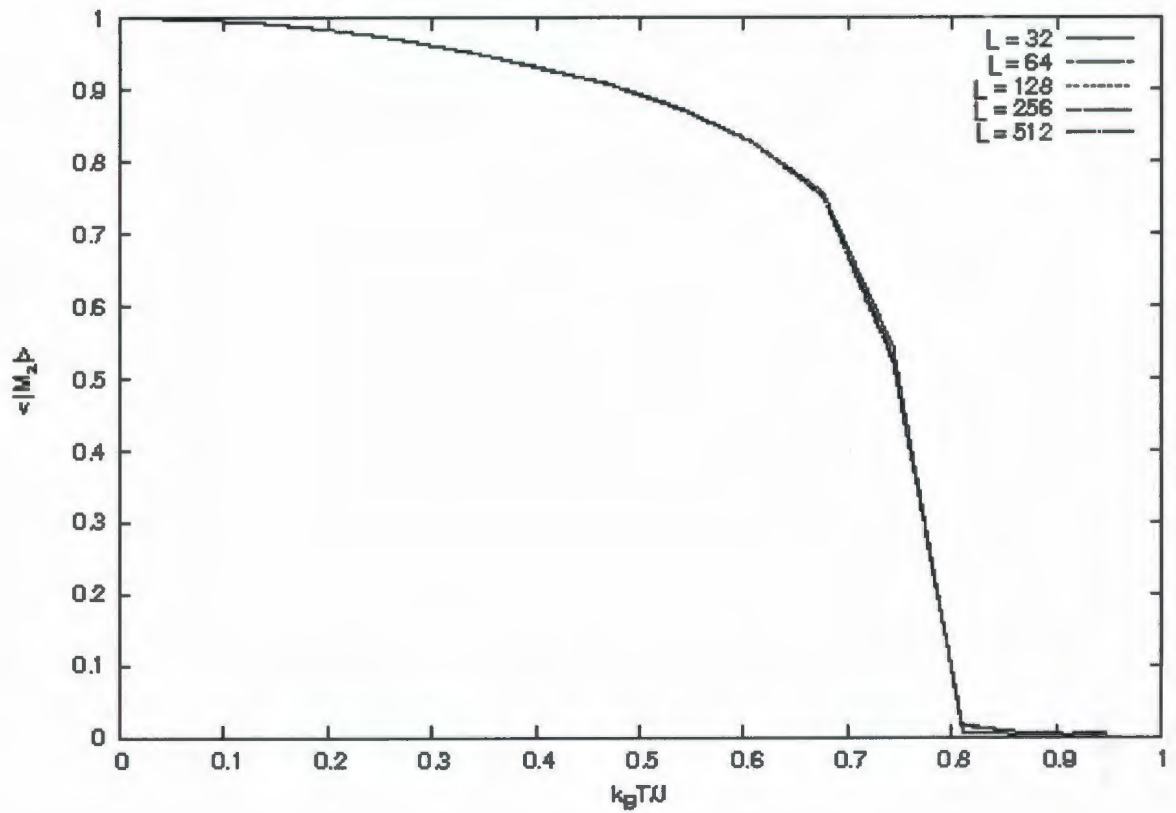


Figure 2.14: Average absolute magnetization as a function of temperature for a $L \times L$ square system of spins. There is a transition to zero magnetization at about $k_B T/J = 0.8$.

Chapter 3

H-T magnetic phase diagrams:

Impact of additional energy terms

Now that we have the ground work completed and the basic LLG model tested, we can begin to examine systems with different geometries of magnetic spins and try to build a model appropriate to explain key features of the magnetic phase diagram of HoMnO_3 .

3.1 Identifying phases and transitions

One of the more difficult problems is to identify, computationally, which of the phases our system is in, given a particular temperature and externally applied magnetic field. We must be able to determine numerically whether or not the system is in the 120° structure in-plane or in some other spin configurations.

While it would be possible to visually inspect all spin configurations individually, this would be completely unmanageable for any practical applications. Any fine changes in structure may be lost, moreover it would be difficult to decide where the

transitions between phases occur. We can achieve an automated 'inspection' through thermally averaged order parameters which are tuned to the structures we expect to see.

3.1.1 Thermal averages within the LLG formalism

An important question to ask now is even if the LLG equations are derived from fundamental considerations, do the dynamics they describe behave according to the laws of thermodynamics? Fortunately this is fairly simple to verify. As it is well known, any infinite physical thermodynamic system must exhibit, over a large a set of randomly sampled states, a sharply peaked energy distribution, centered around the average energy of the system over those states. As this is not an infinite system, we can expect that if LLG can indeed simulate proper thermal averages we will get a broadened but still peaked distribution.

To verify this in our model, we performed simulations on a simple hexagonal stacked lattice with $6 \times 6 \times 6$ spins. For this simulation, the parameters for Eq. 2.1 are $J_a = -1.0$ (antiferromagnetic in-plane), $J_c = 1.0$ (ferromagnetic between planes), and $D = -1.0$ (planar anisotropy). With these parameters, we expect the system to equilibrate to the planar 120° structure. At random time steps after the system equilibrates (which takes about 100 time steps), we calculate the energy of the system and record this using a binning system. Each of the bins contain the counts of system energy within the bin size of $(E_{max} - E_{min}) / N_{bins}$. For our simulation, we use a total of 20 bins. These are plotted on a energy bin versus count graphs, using the middle value of the energy bin as the index. We did this at a temperature of $T = 0.4$ and plotted the results in Fig. 3.1. As can be seen, this shows the expected behaviour for a thermodynamic system. While not shown here, we tested that this occurs for either

a uniform or gaussian number generator in the algorithm to incorporate the thermal noise.

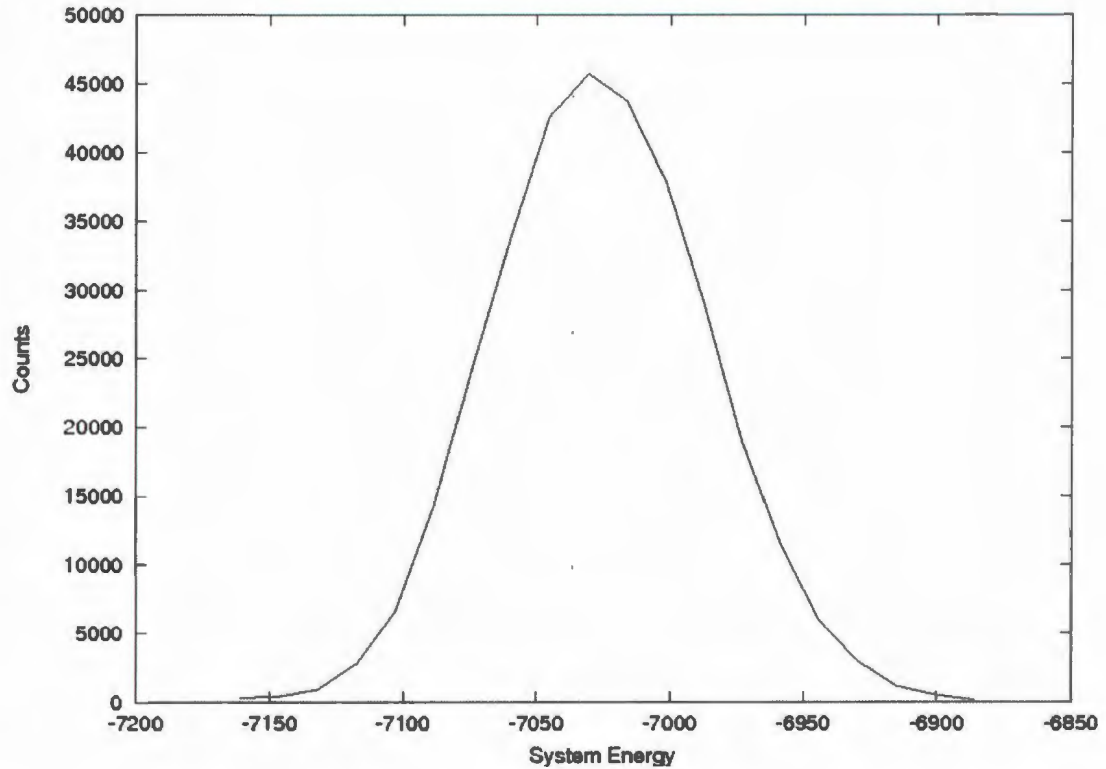


Figure 3.1: An energy distribution curve made using an energy binning method for a simple ferromagnetically stacked system of antiferromagnetic triangular layers from LLG method, using a system size of $6 \times 6 \times 6$. Note how this curve is peaked at a particular point, but is not sharply peaked. This is due to the finite size of the system, yet it still is able to capture most of the energy states around this point.

We now consider taking thermal averages following a similar scheme: run a simulation for a long time and randomly sample the system at various times and take an average of some quantity over this time period. The quantities we wish to consider are the order parameters.

The first of the order parameters has been well studied in frustrated triangular antiferromagnets with the 120° degree structure [15]. We simply call this order pa-

parameter S (different from \vec{S} referring to the vector that represents a spin) and is related to the wave vector, \vec{Q} , that describes the direction of the spin at any given lattice point, \vec{R} . That is:

$$\vec{S}(\vec{R}) = \vec{S}_Q [\exp(i\vec{Q} \cdot \vec{R}) + \exp(-i\vec{Q} \cdot \vec{R})] \quad (3.1)$$

It can be shown that the wave vectors that can describe the 120° structure are:

$$\vec{Q}_1 = \pm \frac{4\pi}{3a} \hat{x}$$

or equivalently

$$\vec{Q}_2 = \frac{2\pi}{3a} \hat{x} \pm \frac{\pi}{b} \hat{y} \quad (3.2)$$

where a is the distance between sites in the \hat{x} direction and b is the distance between sites in the \hat{y} direction. The different values are for the two chiralities which are depicted in Fig. 2.3. Eq. 3.1 can be rearranged and expanded to:

$$\vec{S}_Q(\vec{R}) = (S_x(\vec{R})\hat{x} + S_y(\vec{R})\hat{y}) (\cos(\vec{Q} \cdot \vec{R})) + i (S_x(\vec{R})\hat{x} + S_y(\vec{R})\hat{y}) (\sin(\vec{Q} \cdot \vec{R})) \quad (3.3)$$

This is related to our order parameter S , where:

$$S/N = \sqrt{\sum_{i=1}^N \vec{S}_Q(\vec{R}_i) \cdot \vec{S}_Q(\vec{R}_i)} \quad (3.4)$$

This will take on a value approaching unity at zero temperature when the system is fully ordered in the 120° structure, and approach zero at the transition to paramagnetism due to thermal fluctuations. Figs. 3.2 and 3.3 show how the value of S evolves

as a function of time at a temperature less than and greater than a critical temperature T_c . For this simulation, a simple hexagonal stacked system with $J_a = -1.0$, $J_c = 1.0$ and $D = 1.0$ was used. The simulation results shown in Fig. 3.2 were taken at $T = 0.2$, with a random starting configuration. As can be seen, it starts at a small value and quickly rises to a constant value of about 0.63, where it eventually levels out. We take our thermal averages along this level area of the S/N vs time graph. Above the critical temperature, as shown in Fig. 3.3, the value of S/N hovers around zero.

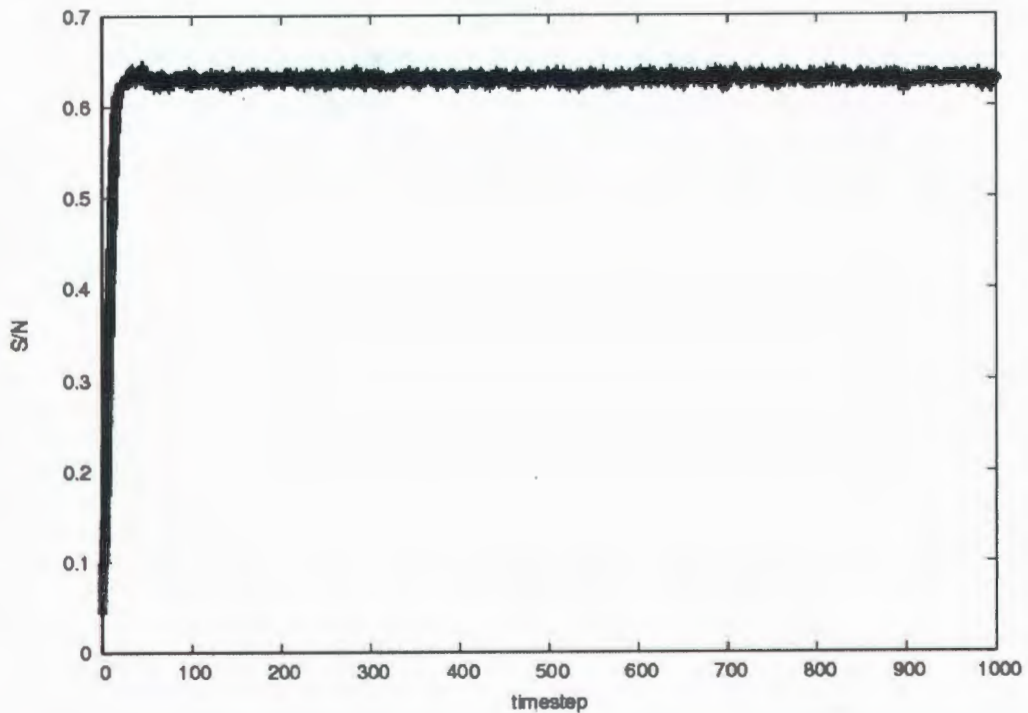


Figure 3.2: S/N versus simulation time, where $N = 6 \times 6 \times 6$, using a simple hexagonal system at a temperature ($T = 0.2$) below the critical temperature. In this case the value of the order parameter quickly levels off and oscillates around a single value.

We take our order parameter measurement as an average over many time steps

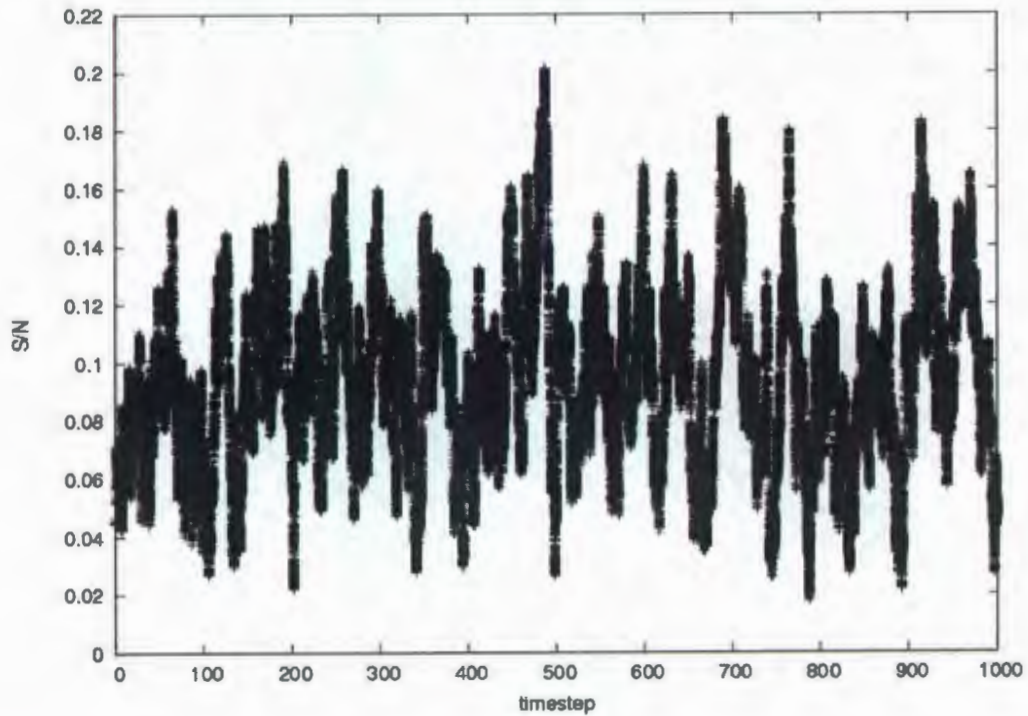


Figure 3.3: S/N versus simulation time, using a simple hexagonal system at a temperature ($T = 1.4$) above the critical temperature. Unlike Fig. 3.2 the order parameter here does not rise and level off to a particular value, but rather stays near zero varying rather wildly.

after the quantity in question is oscillating steadily around a mean value, as this indicates that the system is now in thermal equilibrium. Take Fig. 3.2 as an example; we could begin taking our average after 100 time units, and continue ad infinitum, the more points we take the better the average. If we apply this to a system with the 120 degree structure and take more of these S/N averages at several temperature points at a constant applied field, can determine the transition temperature when our order parameters S heads to zero. This is illustrated in Fig. 3.4, where we take the example of a simple hexagonal system in zero field. We take the transition temperature as the inflection point of the curve as it heads to zero, as is common practice for finite size systems.

It is convenient to define two additional order parameters, M and W . The objective of these order parameters is to determine whether the spins are aligned along the basal plane axes or perpendicular to them. Consider Fig. 3.5, the figure on the left has spins aligned along the basal plane axes while the spins of the figure on the left are perpendicular, as in Fig. 1.3. Consider as an example the following equations:

$$m = \sum_{\Delta} \frac{S_y^2}{S_x^2} \quad (3.5)$$

$$w = \sum_{\Delta} \frac{S_x^2}{S_y^2} \quad (3.6)$$

where the sum is over a triangle of three spins, and S_{α} is the α th component of the spin in the xy plane. Looking at Fig. 3.5 at the second figure, we see that Eq. 3.5 will yield infinity as the upper most spin will have $S_x = 0$, while Eq. 3.6 there is no such division by zero and the sum over the triangle will yield 6. This is a very useful relationship that does exactly what we want. However, it is not efficient to calculate

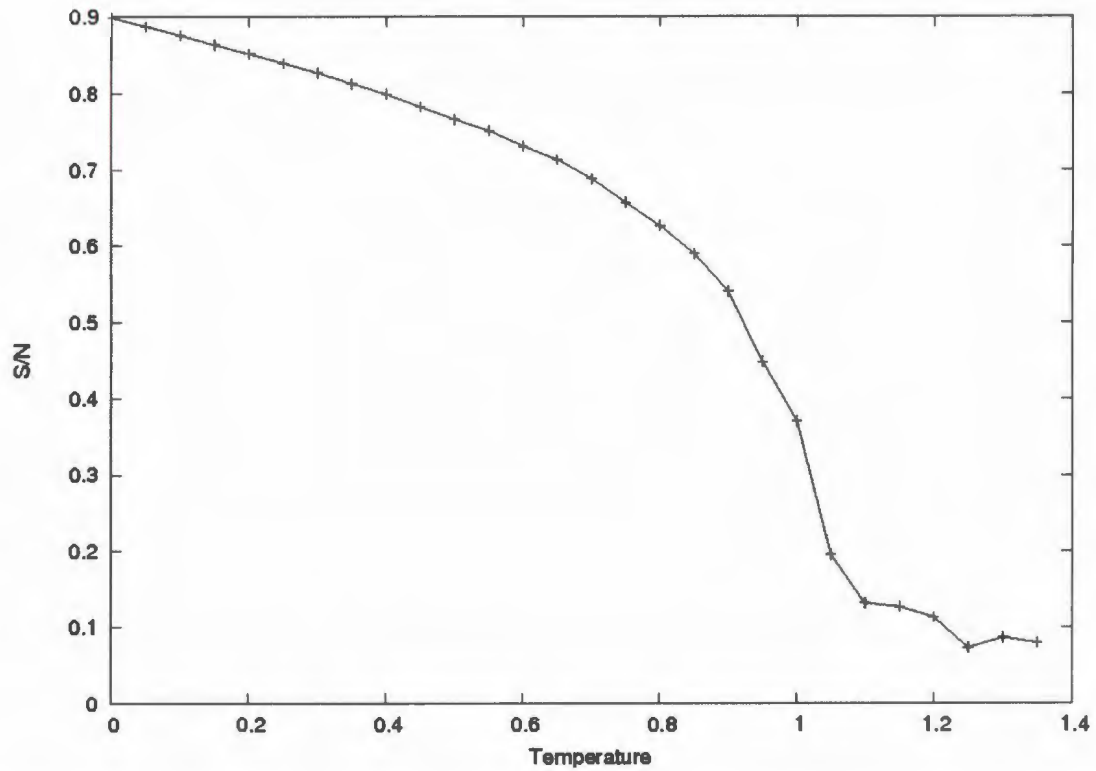


Figure 3.4: An example of how the thermal averaged order parameter S/N behaves as the temperature changes. We define our critical temperature as the point of inflection of the curve before and after the swift drop. In this case the transition temperature would be approximately 1.1.

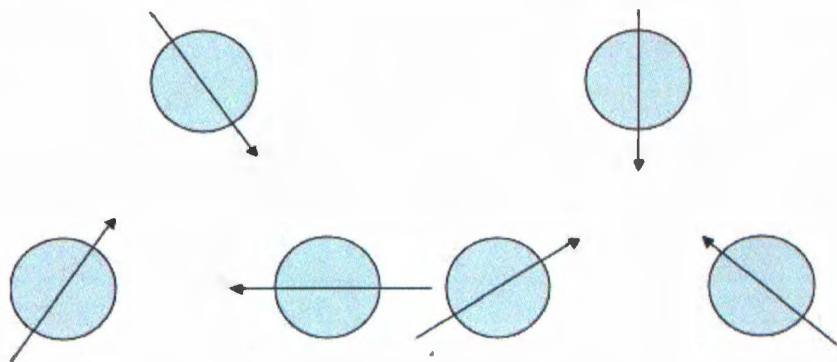


Figure 3.5: The triangle of spins on the left represents spins that are aligned along the basal plane axes, as they are parallel to one of the vectors that joins the centers of two adjacent atoms. On the right is an example of spins aligned perpendicular to those axes. See Fig. 1.3

| | Along Basal* | Perp. to Basal* |
|-----|-----------------------|-----------------------|
| W | $\approx \frac{1}{3}$ | ≈ 3 |
| M | ≈ 3 | $\approx \frac{1}{3}$ |

Table 3.1: Possible empirical values for the order parameters W and M found by applying W and M to systems with spins aligned perpendicular and parallel to the basal plane axes. (* - Basal plane axes).

in this manner. As this involves components of a spin, we should be able to relate these quantities to terms that we calculate for our \vec{S}_{Q1} , the order parameter. We can empirically find that Eq. 3.5 and Eq. 3.6 can be expressed as:

$$W = \sum_i \frac{\text{Im}(S_Q^x)^2}{\text{Re}(S_Q^x)^2} \quad (3.7)$$

$$= \sum_i \frac{\text{Re}(S_Q^y)^2}{\text{Im}(S_Q^y)^2} \quad (3.8)$$

$$M = \sum_i \frac{\text{Re}(S_Q^x)^2}{\text{Im}(S_Q^x)^2} \quad (3.9)$$

$$= \sum_i \frac{\text{Im}(S_Q^y)^2}{\text{Re}(S_Q^y)^2} \quad (3.10)$$

Table 3.1 shows the possible values of M and W found numerically.

Using these three order parameters, we are able to begin explaining the different phases and H - T magnetic phase diagrams of complicated triangular anti-ferromagnets.

3.2 Simple hexagonal systems

Now that we have the tools in place, we can now look at field versus temperature phase diagrams for various spin configurations and signs of J_a and J_c . To begin, we consider at the simplest system that has the 120 degree ordered structure, the simple

hexagonal antiferromagnet. Fig. 3.6 shows an example of such a system, where the spins are arranged in triangular planes stacked directly one over each other. With $J_c = -J_a = 1$, this is the simplest triangular antiferromagnet we can examine and simulate. According to theoretical models, we should get only two phases, an ordered phase with an in-plane 120 degree structure and ferromagnetic order between planes, or a disordered phase. The phase diagram should roughly resemble the sketch in Fig. 3.7.

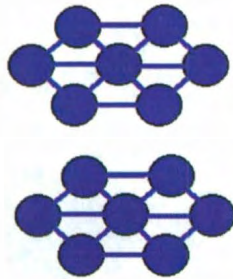


Figure 3.6: This is an example of a simple hexagonal or AA stacked lattice. It consists of triangular planes of spins that are stacked directly on one another.

In theory, the region of order should contain only the 120 degree structure described previously. Because of this, the only order parameter of use is S which will be non-zero when the system is ordered below the transition line and zero above the line. To reproduce the phase diagram illustrated in Fig. 3.9 we must make temperature sweeps at various values of H_z . This yields the results shown in Fig. 3.8.

Taking the point-of-inflection as the transition temperatures at different field values, we can create a phase diagram, shown in Fig. 3.9. From this we can see that the zero field transition temperature T_c is approximately 1.1.

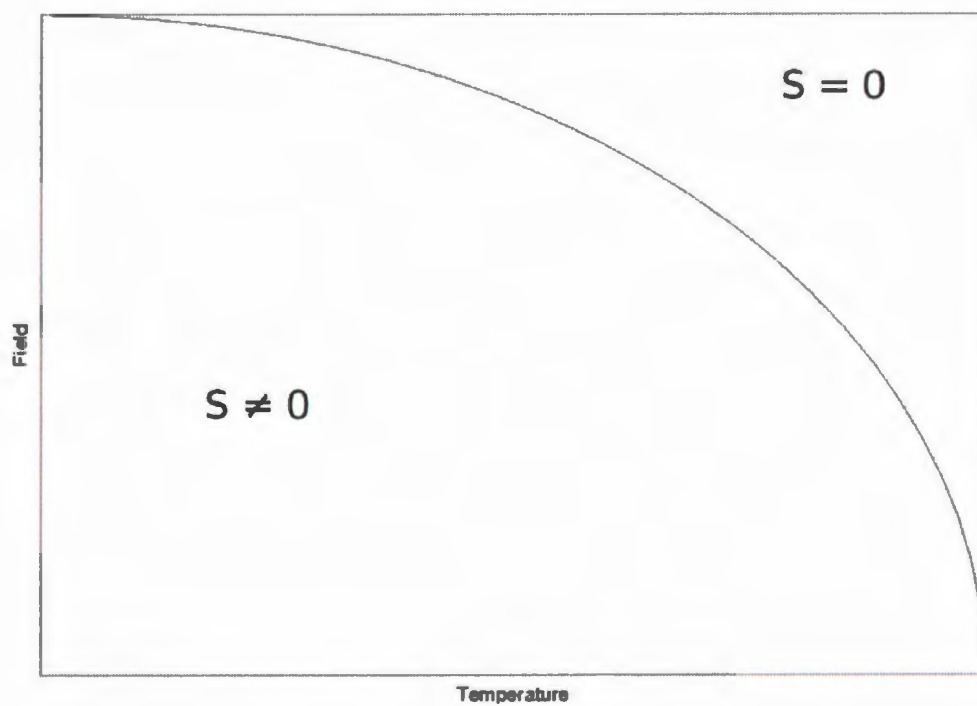


Figure 3.7: Sketch of the anticipated phase diagram for the simple hexagonal antiferromagnet

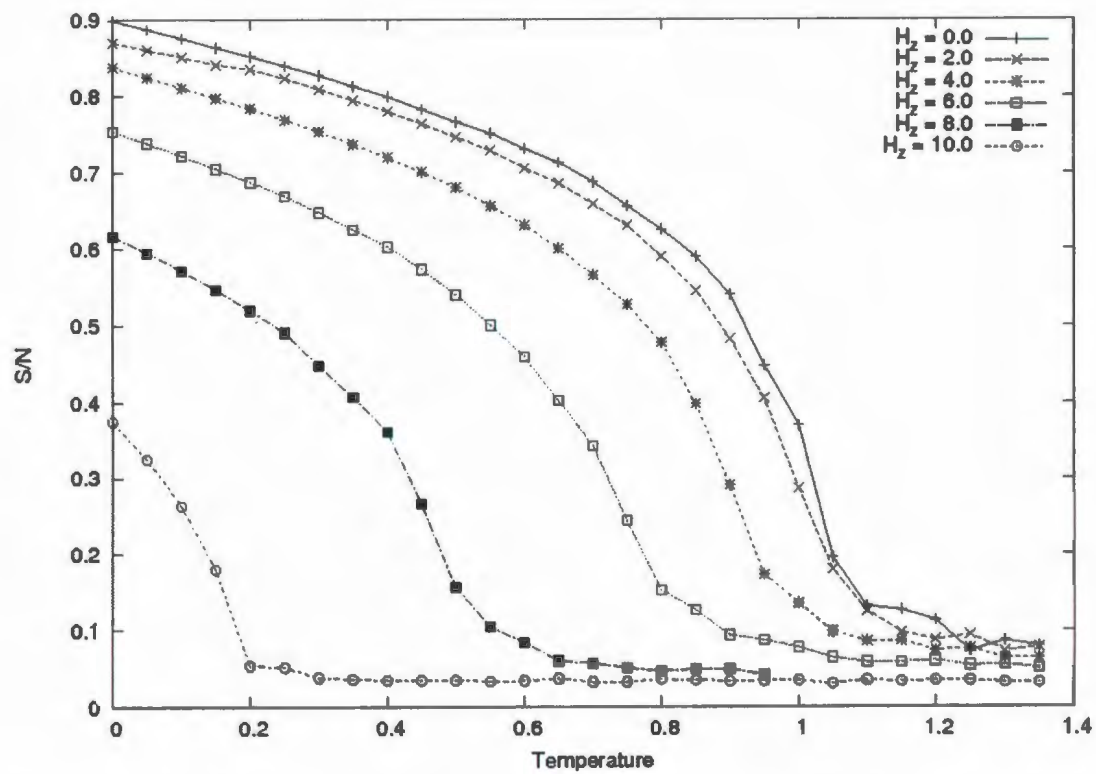


Figure 3.8: Change of the order parameter S/N with varying temperature, at different field values. There is a transition in each curve that represents where there is a phase change from order to disorder. The inflection point of each curve indicates the transition point.

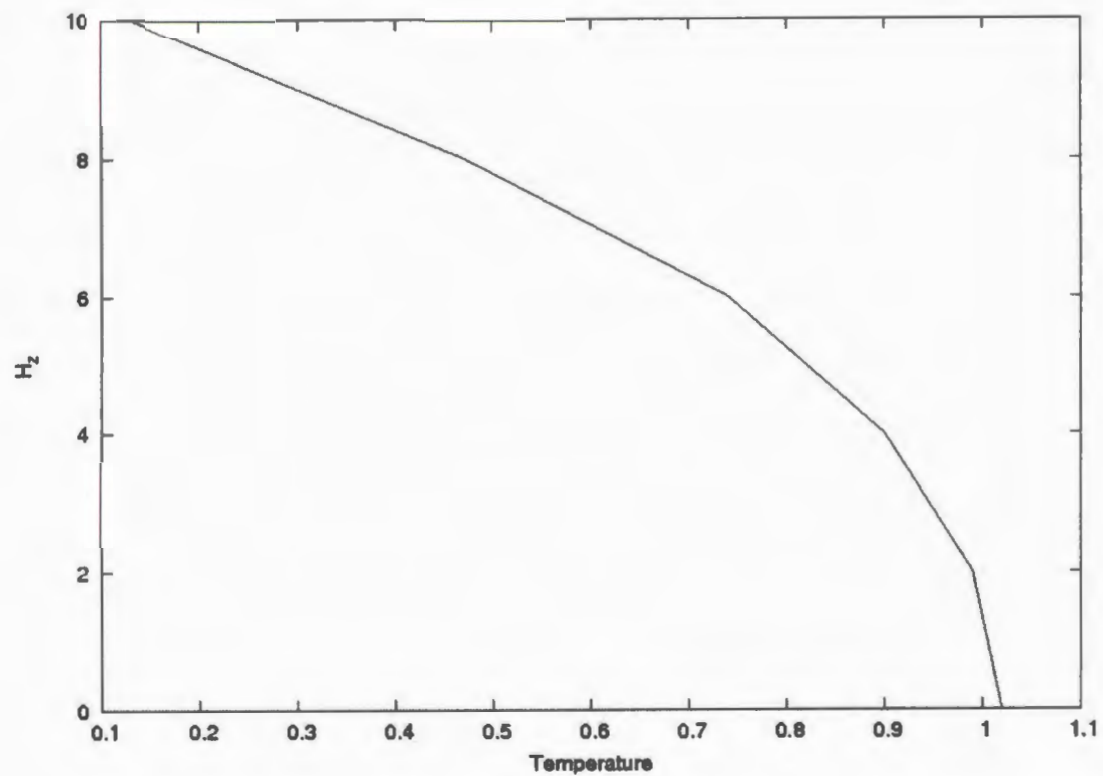


Figure 3.9: Results of taking the transition temperatures from Fig. 3.8 and plotting them against field. We get a phase diagram that is very similar to what was expected from theory (Fig. 3.7). There is a critical temperature of ≈ 1.1 when the applied field is zero. This diagram was generated with $J_a = -1.0$, $J_c = 1.0$ and $D = -1.0$ in our Hamiltonian described in Chapter 2.

3.3 AB stacked system with ferromagnetic and anti-ferromagnetic inter-layer coupling

Another interesting case to consider in the next step toward understanding HoMnO_3 is to model a crystal structure similar to the principal magnetic spins in HoMnO_3 . As discussed in Chapter 1, these Mn ions are arranged on triangular layers stacked in a AB alternating fashion, the Mn ions align with the 'holes' created by the triangular structure of adjacent layers, as shown in Fig. 3.10.

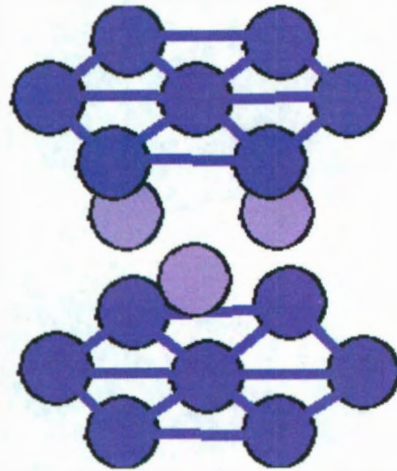


Figure 3.10: Hexagonal AB stacked system where one layer is stacked offset from the first.

This will allow us to get an idea of how well our model mimics the physics of the exchange interactions between Mn atoms in HoMnO_3 (see Fig. 1.3). First, let us examine what structures can be simulated by considering two examples with the inter-layer exchanger parameter, J_c , being either negative or positive at zero magnetic field.

With $J_c > 0$ ($J_c = 0.01$, $J_a = -1.0$, $D = -1.0$, $T = 0.4$) as in Fig. 3.11 we see that the in-plane structure corresponds to the 120 degree configuration as expected,

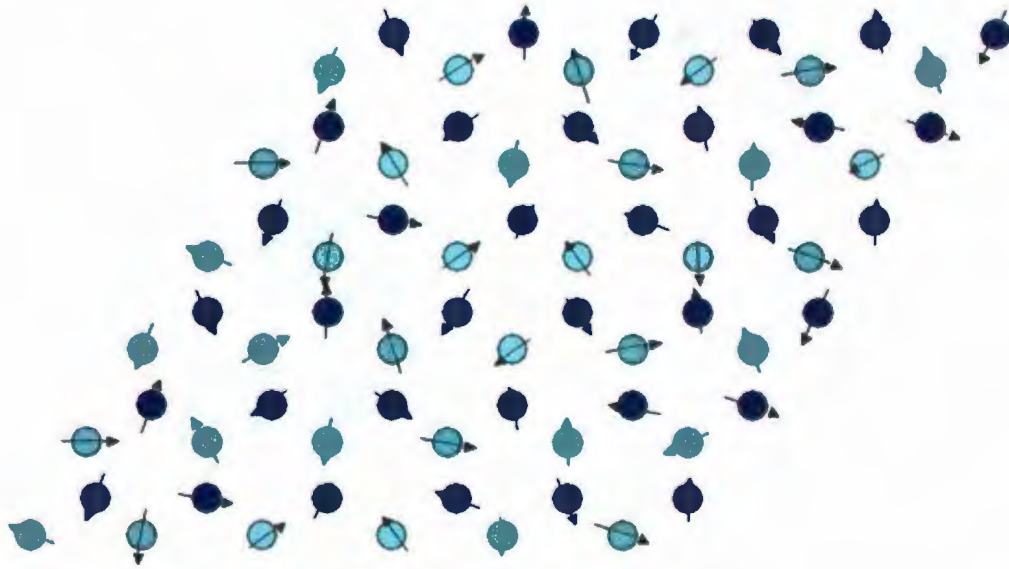


Figure 3.11: A $6 \times 6 \times 2$ system with $J_c = 0.01$, $J_a = -1.0$, $D = -1.0$, $T = 0.4$. Light and dark circles denote AB stacked layers. Notice that while the spins are mostly in the 120° structure, some are off by several degrees and there is no particular orientation of the spins relative to the crystal axis.

with some variation due to finite temperature. However, note that the orientation of the moments in-plane are not tied to the crystallographic axes as in Fig. 1.3. This is what is seen over several simulations and reflects the lack of in-plane anisotropy in our model. The spins between adjacent planes do not line up exactly, as in Fig. 1.3, but can differ by a great angle between planes, or more depending on the size of J_c , presumably due to thermal fluctuations. In this case, the same phenomenon is seen in Fig. 3.12, where $J_c < 0$ ($J_c = -0.01$, $J_a = -1.0$, $D = -1.0$). The spins between planes are not quite antialigned due to the competition between the J_a and J_c energy terms and thermal fluctuations.

The H - T phase diagram of this AB stacked system was mapped out in a fashion similar to the simple hexagonal case. Fig. 3.13 corresponds to the case where $J_c > 0$, and Fig. 3.14 is for $J_c < 0$, both being nearly identical. The transition temperature for both is roughly 0.43. The lower transition temperature, as compared to the simple

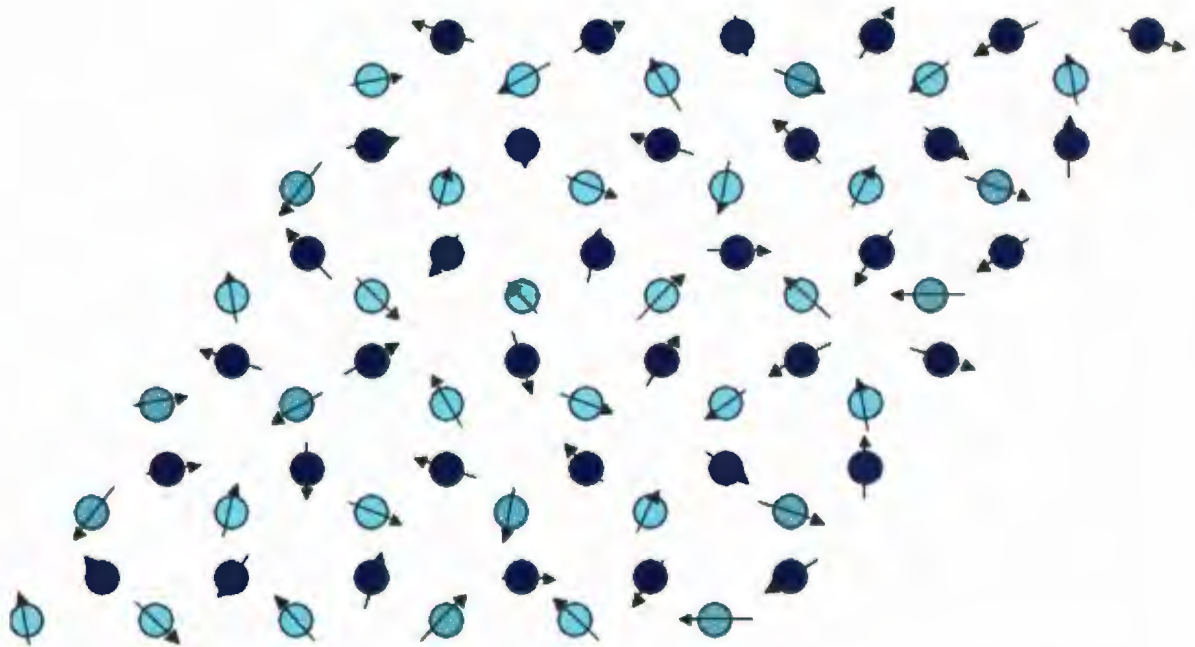


Figure 3.12: A $6 \times 6 \times 2$ system with $J_c = -0.01$, $J_a = -1.0$, $D = -1.0$, $T = 0.4$, as in Fig. 3.11. The 120° structure is again dominant. This time however, the spins are mostly anti-aligned between planes but once again there are some that don't at all due to thermal fluctuations.

hexagonal case (1.1), can be attributed to a weaker interaction between planes. In the simple AA stacked case a single spin \vec{S} has two interplane neighbors, both of which can be parallel with \vec{S} . In the AB stacked case there are six inter-plane neighbors. \vec{S} can only be parallel with two of these spins, one on each plane, if the 120° structure is maintained. Assuming that the planes above and below \vec{S} are the same, the exchange energy term looks like $2J_c\vec{S} \cdot (\vec{S}_1 + \vec{S}_2 + \vec{S}_3)$. It is easy to see that there is no way that all three spins can be parallel if each plane is in the 120 degree structure.

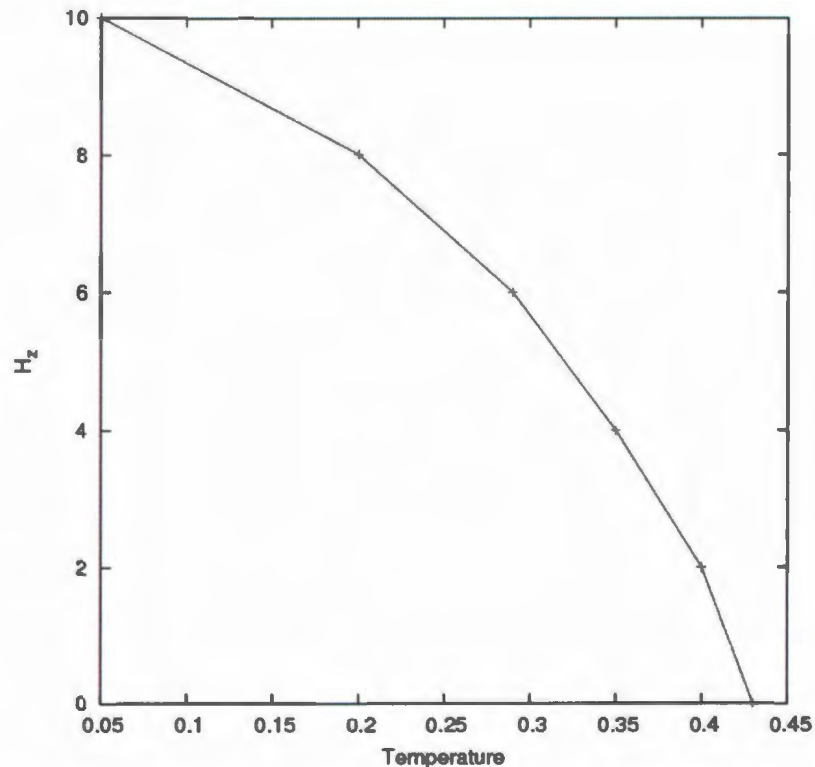


Figure 3.13: AB stacked system with ferromagnetic inter-plane exchange. Using a similar procedure that generated the phase diagram for AA stacking (Fig. 3.9). The critical temperature is around 0.43, less than half the AA stacked case.

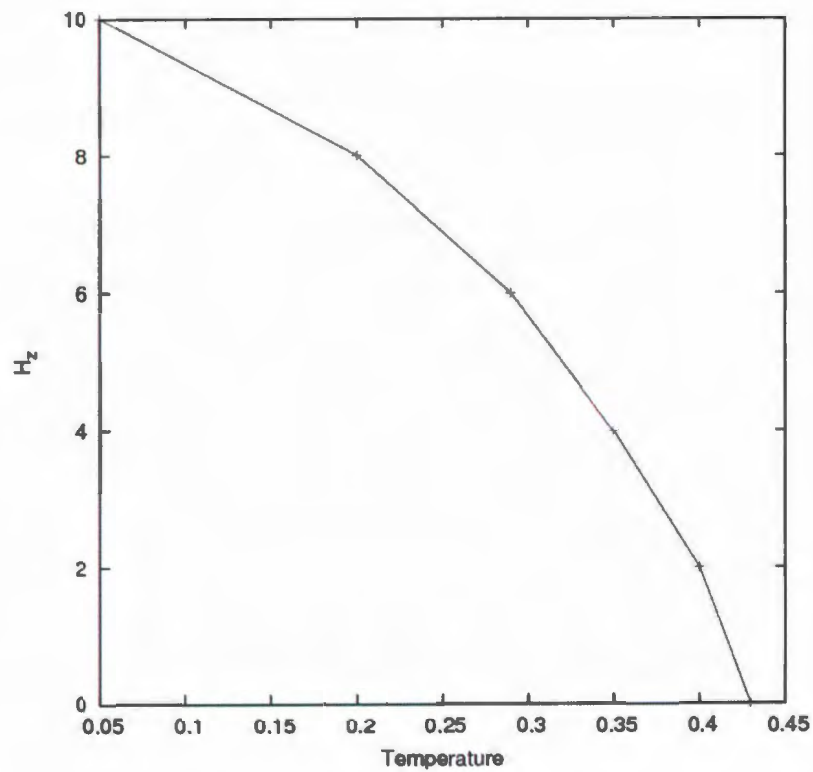


Figure 3.14: For the AB stacked case with antiferromagnetic inter-plane coupling we get the exact same phase diagram as Fig. 3.13. The sign of J_c does not seem to affect the transition temperature of the system and, like the $J_c > 0$ case, the transition temperature is approximately 0.43.

3.4 Effect of in-plane anisotropy

While the interaction terms described in Chapter 2 capture the main features of the HoMnO_3 phase diagram, they are still not enough to completely define each phase. In Fig. 1.3, we see that the spins are either orientated along the basal plane axes or perpendicular. However, with the terms considered so far, we can only reproduce the in-plane 120 degree structure. We need a new term in our Hamiltonian, that will cause the spins to pick out a particular direction with respect to the crystal axes. Hexagonal symmetry allows an anisotropy term of the form [17]:

$$E_6 = E [(S_x + iS_y)^6 + (S_x - iS_y)^6] \quad (3.11)$$

We can express this in terms of the angle that \vec{S} makes with the x -axis, θ (Fig. 2.2) as

$$E_6 = E |S|^6 \cos(6\theta) \quad (3.12)$$

In this form it is easy to see that, depending on the sign of E , that the spins will now want to align either along one of the basal plane axes or perpendicular to them. We see that if:

$$\begin{aligned} E > 0 \quad \text{then} \quad \theta &= (2n + 1) \frac{\pi}{6} \\ E < 0 \quad \text{then} \quad \theta &= (2n) \frac{\pi}{6} \end{aligned}$$

where n is an integer. In other words, when $E > 0$ the spins will tend to align perpendicular to the basal plane axes, while for $E < 0$ they will align parallel. Both configurations are shown in Fig. 3.15.

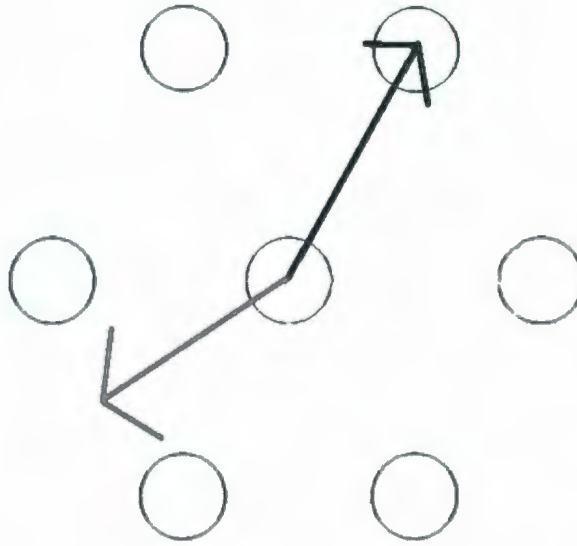


Figure 3.15: Each of the circles represent an atom in the lattice. The dark arrows represent a spin in the xy -plane where $E > 0$ and the spin is aligned with the basal plane axes, where the lighter arrows represent a similar spin where $E < 0$.

With this addition to the Hamiltonian we should be able to account for any of the four magnetic structures described in Fig. 1.3. This is accomplished by changing the signs of the in-plane anisotropy E and the interplane exchange J_c , neither of which change the transition temperature, T_N . We now look at a couple examples where this term is present. The result of adding this term to the Hamiltonian in our LLG simulations are shown in Figs. 3.16 and 3.17 for systems with $E > 0$ and $E < 0$, respectively. Note that the variation of angles between adjacent layers, described in section 3.3, has disappeared. While our model can now generate any of the four observed magnetic structures seen in HoMnO_3 with our model (see Fig. 1.3) depending on the sign of the model parameters, there is still only one transition as there is no mechanism which can induce a transition between those magnetic phases. Consequently, a model with J_{ij} , D , and E , involving only Mn ions, is not adequate to explain the complex magnetic phase diagram of HoMnO_3 .

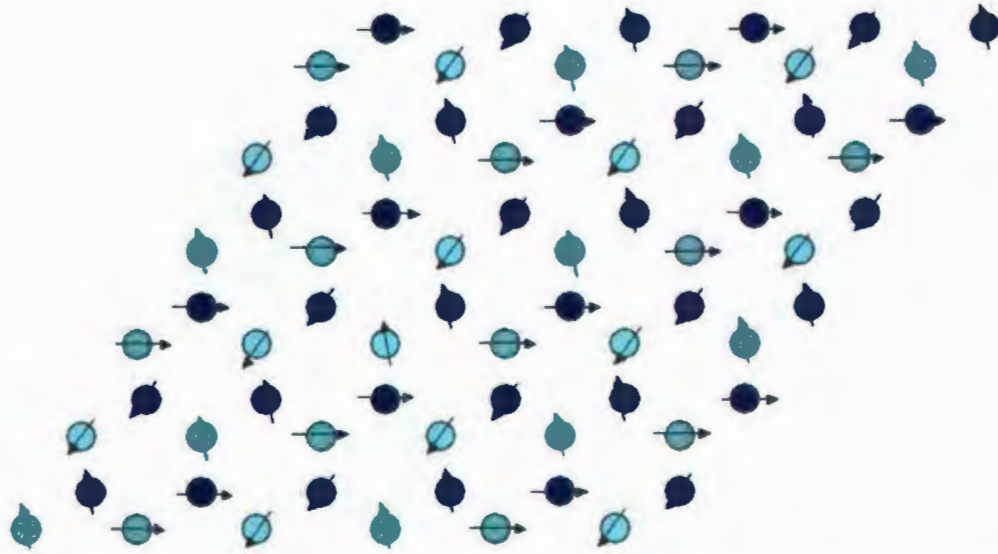


Figure 3.16: With the added $E > 0$ term the spins are now strictly in the 120° structure, with spins aligned parallel to the basal plane axes as Fig. 1.3. This example has ferromagnetic exchange between planes and, as can be seen, the spins are aligned between planes as is expected. This particular structure matches the HT2 phase in HoMnO_3 . Here $J_c = 0.01$, $J_a = -1.0$, $D = -1.0$, $E = 0.01$ and $T = 0.4$.

3.5 Introducing Mn-Ho coupling

It has been suggested that the richness of the HoMnO_3 diagram comes from the interaction between Ho and Mn spins [7]. While the interaction between like atomic spins is well understood, there does not seem to be a universal model of how unlike spins interact, if they do at all.

The interesting thing about HoMnO_3 is that we cannot describe the interaction as a straight exchange term between the Ho and Mn, since they are strictly perpendicular to one another, so any $\vec{S}_{\text{Ho}} \cdot \vec{S}_{\text{Mn}}$ term will be zero. So there must be another way to explain their apparent interaction.

There is an unusual anisotropy term associated with some systems having triangular symmetry such as HoMnO_3 , with space group $P6_3cm$. Called the trigonal term, this interaction may explain the apparent interaction between unlike atoms such as

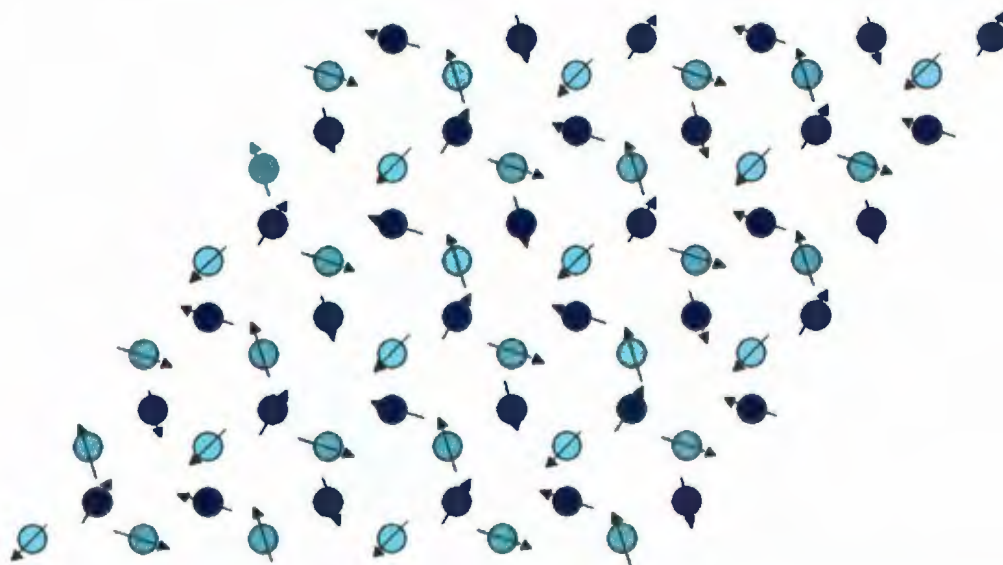


Figure 3.17: An example system with $E < 0$ and $J_c < 0$. Each plane has the 120° symmetry that we would expect, however with $E < 0$ the spin should be aligned perpendicular to the basal plane axes, though the difference between most spins and these axes is slight (it is exaggerated in this diagram as it is otherwise hard to discern with the naked eye). This corresponds to the LT1 phase shown in Fig. 1.3. The spins between planes are anti-ferromagnetically aligned as we expect with negative J_c . Here $J_c = -0.01$, $J_a = -1.0$, $D = -1.0$, $E = -0.01$ and $T = 0.4$.

Ho and Mn. However, it is only allowed by the magnetic symmetry if either the Mn spins or the Ho spins are antiferromagnetically aligned between layers, but not both, or the term will be zero. This term has had previous applications to other materials [17] in various forms, but for our purposes it could be of the form:

$$K \sum_{\text{Mn, Ho}} \{ S_{\text{Ho}}^z S_{\text{Mn}}^y [3 (S_{\text{Mn}}^x)^2 - (S_{\text{Mn}}^y)^2] \} \quad (3.13)$$

Explicit Mn-Ho coupling has not been included in our LLG simulations. However, we consider a simple Landau free energy model with this term included in the following chapter.

Chapter 4

Discussion on the effects of magnetic Ho ions

While this work does not fully explain the the phase diagram of HoMnO_3 , it demonstrates some progress toward understanding the important magnetic interactions in this material. We are able to simulate and generate every experimentally observed configuration through just a few interaction terms. While we do see a transition between the ordered phase that is defined by our model parameters and a disordered phase, transitions between ordered phases do not occur.

We have also shown that LLG can be used to find not only zero temperature steady state configurations but also spin configurations in frustrated triangular anti-ferromagnets at a finite temperature. These configurations show real thermodynamic properties, which can be used to define the aforementioned phase transitions.

The trigonal K term is next to be explored and looks very promising. In section 4.1, a simple Landau free energy is presented and a brief example is given on what is to be expected when this term is added to a model such as ours. In section 4.2, a discussion on other possible Mn-Mn, Ho-Ho and Mn-Ho exchange interactions is

given.

4.1 Simple Landau free energy

An analysis of a simple Landau free energy which includes Mn-Ho coupling through the trigonal K term, can show us roughly the types of transitions that are possible between different phases. It is based on the exchange energy terms as in our Hamiltonian, however we also have two different spin entities $\vec{S} = \vec{S}_{\text{Mn}} \perp \hat{c}$ and $\vec{S}_o = \vec{S}_{\text{Ho}} \parallel \hat{c}$ which couple through the trigonal term. Eq. 4.1 is the zero field Landau free energy with isotropic terms to sixth order and anisotropy terms as discussed above can be written as [21]:

$$F = AS^2 + A_o S_o^2 + \frac{1}{2}BS^4 + \frac{1}{2}B_o S_o^4 + B_1 S^2 S_o^2 + \frac{1}{3}CS^6 + K S_o S^3 \cos 3\phi + ES^6 \cos 6\phi \quad (4.1)$$

where ϕ is the angle \vec{S} makes with the \hat{a} axis, $A = a(T - T_N)$, $A_o = a(T - T_o)$, and the other constants are free parameters.

Assuming reasonable parameter values, we can numerically minimize the free energy. With $a = 1$, $T_o = 1$, $T_N = 1$, $B = 1$, $B_o = 0.3$, $B_1 = \frac{1}{2}$, $C = 1$, $E = 0.2$, $K = 0.2$, results show a total of 3 transitions. Referring to Fig. 4.1, below $T = 0.45$ we see a phase with $P6'_3$ symmetry, that has ϕ between 0 and $\frac{\pi}{2}$. At $T = 0.45$, a transition to the HT1 phase ($\phi = \frac{\pi}{2}$) is realized while at and at $T = 0.65$ we see a transition to the HT2 phase ($\phi = 0$) is reproduced, as in Fig. 1.3.

While this analysis depends heavily on the initial parameters, it shows that it is possible to generate more than one transition with the trigonal term as a consequence of Mn-Ho coupling.

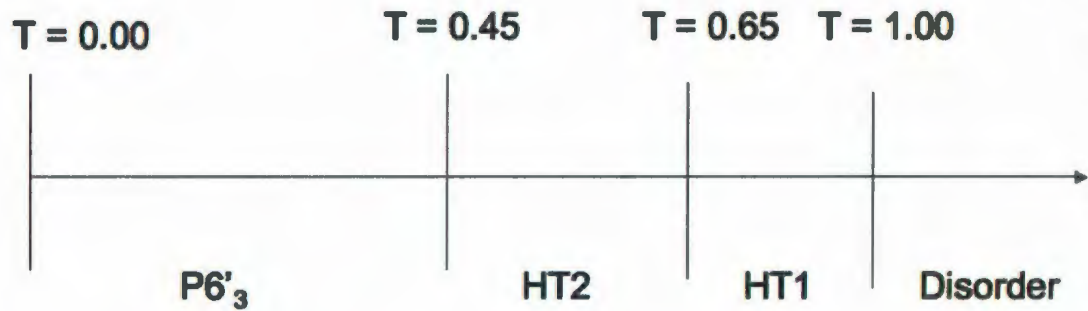


Figure 4.1: Landau theory results at $H = 0$

4.2 More interactions in HoMnO_3

The model we have developed thus far for HoMnO_3 assumes a perfect triangular lattice. This is in fact an approximation, as the structure HoMnO_3 , particularly the Mn spins, is composed of slightly distorted triangles [16]. These distortions will lead to two or more unequal in-plane exchange terms depending on how the lattice differs from that of the perfect triangular lattice (an example of which is in Fig. 4.2).

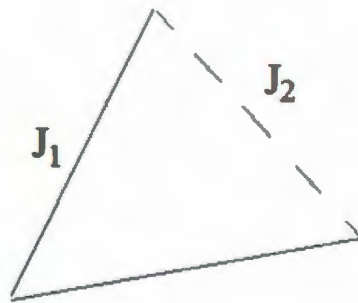


Figure 4.2: The triangular lattice in the structure of HoMnO_3 is in reality, a slightly distorted triangular lattice

When putting HoMnO_3 under close inspection, we notice that there are many types of interactions that are relevant, some of them being the exchange between magnetic spins. In Chapter 3, we touched on a few possible interactions in order to

| Interaction | In plane or Between | NN distance (Å) | Number in Fig 4.3 |
|---|---------------------|-----------------|-------------------|
| Ho ₂ - Mn | Between | 3.5049 | 1 |
| Mn - Mn | In plane | 3.5334 | 2 |
| Ho ₁ - Ho ₂ | In plane | 3.5334 | 3 |
| Ho ₁ - Ho ₁ | In plane | 6.1200 | 4 |
| Ho ₁ - Mn | Between | 3.5049 | 5 |
| Ho ₁ - Ho ₂ | Between | 6.7063 | 6 |
| Ho ₂ - Ho ₂ | In plane | 3.5334 | 7 |
| Mn - Mn | Between | 3.5049 | 8 |
| Ho _(1,2) - Ho _(1,2) | Between | 5.700 | 9 |

Table 4.1: A number of the possible dominant interactions in HoMnO₃, see Fig. 4.3 for an example.

model the H - T magnetic phase diagram. However, there are a host of other possible exchange interactions as listed in Table 4.1 and illustrated in Fig. 4.3.

There is a possibility of 9 dominant interactions between spins in HoMnO₃, however, so far this work has only examined the effect of exchange between Mn-Mn in-plane and out of plane. While this is enough to describe all phases mentioned in various papers, it is not enough to account for a transition between any ordered phases. This is attributed to the fact that we assume a perfect triangular lattice on each plane. If we must take into account the irregularity described in Fig. 4.2, this will change a number of distances between atomic spins and will require even more exchange or anisotropy terms.

To complete the phase diagram of HoMnO₃, Ho spins must be added to the model, as explained in Section 3.5. In addition to the exchange term in Eq. 3.13, we must bring two new atomic spins into our LLG equations (Ho₁ and Ho₂). One way to accomplish this is to have separate exchange and anisotropy terms in our hamiltonian for each Mn, Ho₁, and Ho₂. The difficulty will be to estimate which of the additional interactions in Table 4.1 are important.

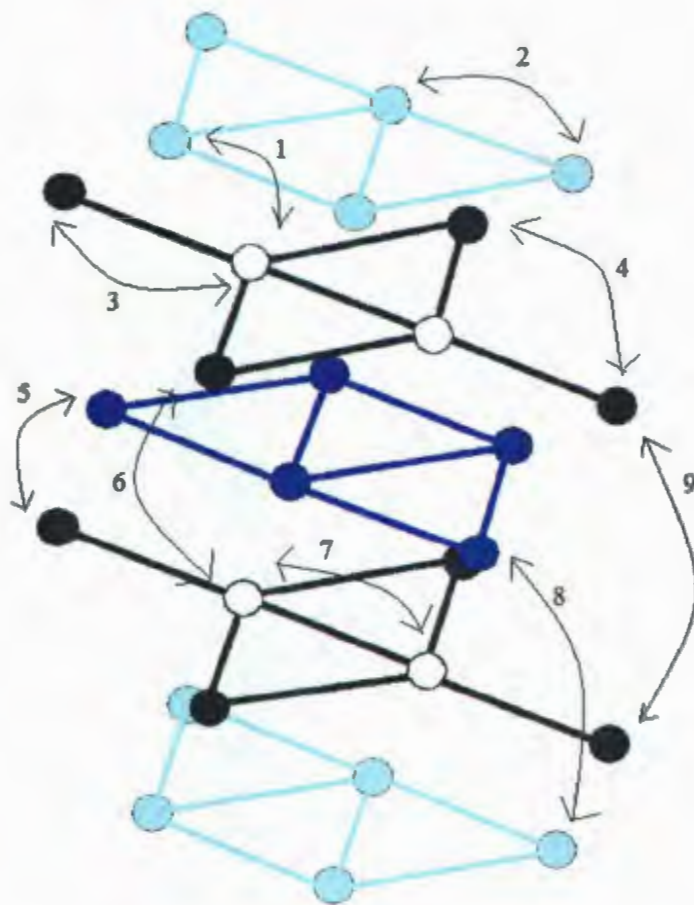


Figure 4.3: A diagram showing all interactions explained in Table 4.1. Labels refer to the right hand column of the same table.

Chapter 5

Summary and Conclusions

One of the most important conclusions we can draw from results presented in this thesis is the fact that we can accurately model geometrically frustrated antiferromagnets with the Landau-Lifshitz-Gilbert equations, as long as we have an accurate Hamiltonian. In Chapter 2, using a typical cubic antiferromagnetic lattice we were able to reproduce the energy behavior versus field, which was used to compare the speed and accuracy between the EFM and LLG methods. In our studies of hexagonal frustrated anti-ferromagnets, we obtain the 120 degree structure common to these systems, whenever the spins are restricted to the plane.

Using the LLG method, we were able to model phase transitions due to temperature and applied magnetic field in several stacked triangular antiferromagnets. In these systems there was only one ordered phase with a single transition to a disordered state. The ordered phase depends on how the hexagonal planes are stacked, as well as, the signs of the inter-plane exchange and the in-plane anisotropy terms. The in-plane anisotropy term is needed to explain all of the HoMnO_3 structures, but it is not enough to account for all transitions in the HoMnO_3 H - T phase diagram.

Our model considers the Mn spins as the only contributor to the spin structure.

The next important step toward understanding and modeling the entire phase diagram of HoMnO_3 is to include interactions between Ho spins, as well as with Mn spins. Using a simple Landau model, we were able to show that the trigonal term could account for different phase transitions at zero field and shows that the same structures, described in experimental work on HoMnO_3 , come out of energy minimization.

Another idea for future work is to deepen the understanding of the AB hexagonally stacked system, particularly when in-plane anisotropy has been added to the system. It is easy to see empirically that large exchange between planes (that on the order of the in-plane exchange) is in competition with the effects of in-plane anisotropy, and large in-plane anisotropy negates the effects of the in-plane exchange. While this has not been explored at all in this work, it would help with the understanding of what reasonable values for the in-plane anisotropy and the inter-plane exchange terms, which in turn will help the understanding of the interactions of HoMnO_3 and others in the RMnO_3 family which all have the same crystal structures.

Appendix: Addition of Temperature to LLG

A quantity (X) that propagates with a time step Δt in a random (stochastic) fashion is called a Markov process [18]. Thus, the change in X can be defined by:

$$X(t + \Delta t) = X(t) + F[X(t), \Delta t] \quad (5.1)$$

where F is some normal random propagator called the Markov propagator. The Weiner process describes a continuous stochastic change over a time Δt which can be described in terms of a Markov propagator [19]:

$$F[X(t), \Delta t] = \delta\sqrt{\Delta t}N_{\Delta t}(0, 1) \quad (5.2)$$

where δ is a variable that defines the size of the propagation over Δt , and $N_{\Delta t}(0, 1)$ is a normal random number centered around 0 with deviation 1. This type of description is also responsible for Langevin dynamics. The factor of $\delta\sqrt{\Delta t}$ comes from the normalization of the assumed Gaussian distribution of the probability density of a stochastic variable X at time t in:

$$P(X, t) = \frac{1}{\sqrt{2\pi\delta^2 t}} \exp\left[-\frac{(X - X_0)^2}{2\delta^2 t}\right] \quad (5.3)$$

This also satisfies the classical diffusion equation with the diffusion constant being $\frac{1}{2}\delta^2$. We can now look at a change of X with respect to time:

$$\frac{dX}{dt} = \frac{X(t + \Delta t) - X(t)}{\Delta t} = \frac{\delta}{\sqrt{\Delta t}} N_{\Delta t}(0, 1) \quad (5.4)$$

Taking this back to the problem of adding temperature to the LLG equation, we want to change the spin so the change is proportional to the temperature. We can model this using a small random torque, $\vec{\tau}$, in a similar way to how the torque due to effective field affects the spin:

$$\vec{\tau} = -\vec{S} \times \vec{\eta} \quad (5.5)$$

$$\vec{\eta} = \eta [N_x(0, 1), N_y(0, 1), N_z(0, 1)] \quad (5.6)$$

$$(5.7)$$

where $N_i(0, 1)$ are all statistically independent. The η is a constant that is proportional to the temperature, the proportionality is determined from equipartition theorem and fluctuation-dissipation theorem [20]:

$$\eta = \sqrt{4\tilde{\alpha}k_B T} \quad (5.8)$$

$$\tilde{\alpha} = \frac{\alpha\gamma}{1 + \alpha^2} \quad (5.9)$$

Now looking at the change of \vec{S} with respect to time, and making use of Eq. 5.4, we

now have:

$$\frac{\vec{S}(t + \Delta t) - \vec{S}(t)}{\Delta t} = \frac{\vec{\tau}}{\sqrt{\Delta t}} \quad (5.10)$$

$$\vec{S}(t + \Delta t) - \vec{S}(t) = -\sqrt{\Delta t} \vec{S} \times \vec{\eta} \quad (5.11)$$

With this, the damped LLG equation (Eq. 2.19) becomes:

$$\vec{S}(t + \Delta t) = \vec{S}(t) - \frac{\Delta t \gamma}{1 + \alpha^2} [\vec{S} \times \vec{H}_{\text{eff}} + \alpha \vec{S} \times (\vec{S} \times \vec{H}_{\text{eff}})] - \sqrt{\Delta t} \vec{S} \times \vec{\eta} \quad (5.12)$$

So, to impliment this into a computer code, we need three independent random numbers. As long as a good pseudo random number generator, with a long enough repetition length, is used any three generated numbers should be independent. These will be multiplied by the η corresponding to the temperature of interest (Eq. 5.8) and stored in a vector. In the interest of using an adaptive time step, this new temperature term must be subtracted at the end of each step rather than being a part of the adaptive time step. This is because we generate a new random vector with each configuration so achieving convergence with a random term is highly unlikely.

Bibliography

- [1] M. Fiebig, *Revival of the magnetoelectric effect*, J. Phys. D, **16** R123 (2005).
- [2] T. Kimura, *Spiral Magnets as Magnetoelectrics*, Annu. Rev. Mater. Res. **37** 387 (2007).
- [3] F. Yen, et al., *Magnetic Phase Diagrams of Multiferroic Hexagonal $RMnO_3$ ($R=Er, Yb, Tm, \text{ and } Ho$)*, J. Mater. Research, **22** 2163 (2007).
- [4] M. Fiebig, and C. Degenhardt, *Magnetic phase diagram of $HoMnO_3$* , J. Appl. Phys., **91** 8867 (2002).
- [5] A. Muñoz, et al., *Evolution of the Magnetic Structure of Hexagonal $HoMnO_3$ from Neutron Powder Diffraction Data*, Chem. Mater., **13** 1497 (2001).
- [6] P. J. Brown, and T. Chatterji, *Neutron diffraction and polarimetric study of the magnetic and crystal structures of $HoMnO_3$ and $YMnO_3$* , J. Phys.: Cond. Matt., **18** 10085 (2006).
- [7] S. Nandi, et al., *Nature of Ho Magnetism in Multiferroic $HoMnO_3$* , Phys. Rev. Lett., **100** 217201 (2008).
- [8] Neil Ashcroft, and N. Mermin, *Solid State Physics* (Brooks/Cole, Pacific Grove, CA) (1976).

- [9] L. R. Walker, and R. E. Walstedt, *Computer model of metallic spin-glasses*, Phys. Rev. B, **22** 3816 (1980).
- [10] B. Heinrich, and C. Bland, *Ultrathin Magnetic Structures IV* (Springer, New York, NY) (2005).
- [11] C. Kittel, *Introduction to Solid State Physics*, (Wiley Publishing, Hoboken, NJ) (1976).
- [12] Kai Yosida, *Theory of Magnetism* (Springer, New York, NY) (1991).
- [13] Jason Mercer, private communication.
- [14] William Brown, *Micromagnetics* (Krieger Publishing Company, Malabar, FL) (1963).
- [15] M. L. Plumer, and A. Caillé, *Nonlocal Landau free-energy functional: Application to the magnetic phase transition in CsNiF₃*, Phys. Rev. B., **37** 13 7712 (1988).
- [16] I. Munawar, and S. H. Curnoe, *Theory of magnetic phases of hexagonal rare earth manganites* J. Phys.: Condens. Matter, **18** 9575 (2006).
- [17] J. Jensen, and A. Mackintosh, *Rare Earth Magnetism: Structures and Excitations*, (Clarendon Press, Oxford) (1991).
- [18] Alexandre Chorin, *Stochastic Tools in Mathematics and Science* (Springer, New York, NY) (2006).
- [19] Fima Klebaner, *Introduction to Stochastic Calculus with Applications* (Imperial College Press, London) (2005).
- [20] John Whitehead, private communication.

[21] Martin Plumer, private communication.

